



RESEARCH ARTICLE

10.1029/2021MS002637

Key Points:

- Newly developed functionality for continuously temporally updated Ensemble of Data Assimilations (EDA) system to estimate B-matrix for a high resolution European reanalysis
- B-matrix successfully estimates weather regime change but observation network and proportions of EDA forecast difference sourcing are vital
- Demonstrated improvements in statistical profiles of B-matrix with some improvements in forecast scores and Copernicus European Regional Re-Analysis (CERRA) system performance

Correspondence to:

A. El-Said,
adam.el-said@meteo.fr

Citation:

El-Said, A., Brousseau, P., Ridal, M., & Randriamampianina, R. (2022). Towards full flow-dependence: New temporally varying EDA quotient functionality to estimate background errors in CERRA. *Journal of Advances in Modeling Earth Systems*, 14, e2021MS002637. <https://doi.org/10.1029/2021MS002637>

Received 1 JUN 2021

Accepted 7 JAN 2022

Author Contributions:

Formal analysis: A. El-Said

Supervision: A. El-Said

Towards Full Flow-Dependence: New Temporally Varying EDA Quotient Functionality to Estimate Background Errors in CERRA

A. El-Said¹ , P. Brousseau¹, M. Ridal² , and R. Randriamampianina³

¹Metéo-France, CNRM-GMAP, Toulouse, France, ²Swedish Meteorological and Hydrological Institute, Norrköping, Sweden,

³Norwegian Meteorological Institute, Oslo, Norway

Abstract A new temporally evolving quotient on the Ensemble of Data Assimilations (EDA) technique for estimating background error covariances has been developed for the Copernicus European Regional Re-Analysis (CERRA). The B-matrix is modeled on a bi-Fourier limited area model. Background errors are assumed isotropic, homogeneous and non-separable. Linearized geostrophic and hydrostatic balances are incorporated as multivariate relationships, coupling vorticity, and geopotential extended to mass-wind and specific humidity fields via the f -plane approximation. The EDA comprises two main pools: seasonal and daily. The seasonal component comprises winter and summer EDA forecast differences at reanalysis resolution (5.5 km). The new time quotient function temporally changes the mixture of differences from each season, to make up the seasonal component. The daily component is an 11 km moving 2.5 days average changing in real-time. Subsequent B-matrix computation sees the ingestion of forecast differences from both components, with a fixed split of 80%–20% seasonal-daily, every 2 days. The sourcing of these forecast differences from both seasonal and daily sources is in continuous temporal flux therefore. We consider a case study to illustrate the potential of estimating weather regime change using CERRA-EDA with varying proportions of seasonal-daily mixing, while including settings used for CERRA production. Our case study shows that the most influential factors are differences in observation networks between the given years, their spatial distribution across the CERRA domain, and the proportion of seasonal-daily split. It is shown that our method provides improvement over a static B-matrix.

Plain Language Summary The Copernicus European Regional Re-Analysis (CERRA) is a “second look” at the evolution of weather over Europe and North Africa between 1984 and 2021. This “re-analysis” merges state-of-the-art observations with regional weather model data. The re-analysis is performed long after the fact, after previous predictions, using data at that time. The quality of the reanalysis is highly dependent on the errors in the previous forecast (B). No computer on Earth is capable of storing the mammoth B-matrix explicitly. A subset of prognostic variables (specific humidity, temperature and surface pressure, vorticity and divergence) are used to represent the weather, and simplistic assumptions of their error structures are made in order to quantify B. To this end, their statistical tendencies are obtained using forecast differences from an Ensemble of Data Assimilations (EDA). Each EDA member is an independent analysis using the same data but perturbed observations. The structure of B assumes: linearized meteorological balances with respect to the Earth's rotation and vertical motion, and the positional and directional distribution of errors are horizontally uniform (equally spread), while the vertical is governed by the vertical pressure profile. This roughly resembles a deformed tear-drop. In this paper, we augment the established EDA method in estimating our B matrix with our assumptions to demonstrate its large-scale regional estimation capability against the EDA method without our new augmentation.

1. Introduction

A new system delivering the Copernicus European Regional Re-Analysis (CERRA) has been developed, provided primarily by the Swedish Meteorological and Hydrological Institute (SMHI) in collaboration with Météo-France and Met Norway. The CERRA system uses “Hirlam Aladin Research Mesoscale Operational Nwp In Europe” (HARMONIE), where the physics and dynamics are handled by “Aire Limitée Adaptation dynamique Développement InterNational” (ALADIN). The CERRA reanalysis period spans 1984–2021 and covers Europe and the North of Africa as shown in Figure 2. HARMONIE is currently in operational use by the HI-Res Limited

© 2022 The Authors.

This is an open access article under the terms of the [Creative Commons Attribution-NonCommercial License](#), which permits use, distribution and reproduction in any medium, provided the original work is properly cited and is not used for commercial purposes.

Area Modeling (HIRLAM) consortium across 26 countries in Europe and northern Africa for short-range mesoscale NWP.

Retrospective analyses (reanalyses) provide temporally continuous and spatially coherent descriptions of atmospheric model states over a long time-frame. The practice is now commonplace for large weather centers since their advent 40 years ago for the First Global atmospheric research program Global Experiment (FGGE), Bengtsson et al. (1982). The temporal span of global reanalysis ranges between 10 years (ERA-15 for example) to nearly 120 years (ERA20C, Poli et al. (2016)). The research community's use of reanalyses continues to grow worldwide as the scope of its use reaches into policy making, the energy sector, agriculture, education and other economic markets. At the time of writing, this paper Google scholar quotes in excess of 30,000 citations for NCEP/NCAR's 40-year reanalysis, Bromwich and Wang (2005), and 19,000 for ECMWF's outgoing ERA-Interim, Dee et al. (2011). Global reanalyses also feed into more specialized regional reanalyses. Regional reanalyses add clarity with increased resolution and increasingly bespoke orography, dynamics and physics considerations, as spatio-temporal resolution increases. Upcoming specialist and regional reanalyses in Europe provided under the Copernicus Climate Change Services (C3S) framework include Copernicus Arctic Regional Reanalysis (CARRA) and CERRA-Land.

The background error covariance matrix is a vital component of any DA system. This importance carries over into a DA system for regional reanalysis, but B-matrix calibration and estimation takes a slightly different tone to that of shorter time-scaled weather prediction applications. The B-matrix spreads information presented by the observations over the analysis increment. It does this by providing statistically consistent increments to the neighborhood of grid-points at all levels of the model for modeled variables. Second, it tries to ensure that observations of model variables, temperature for example, produce dynamically consistent increments across other model variables, such as wind and humidity. Cardinali et al. (2004) illustrated with the ECMWF boreal spring 2003 operational system, that 15% of the global influence is due to the assimilated observations in any one analysis, and the complementary 85% is the influence of the information from the B-matrix, a short-range forecast containing information from earlier assimilated observations. Further to this, 25% of the observational information was provided by surface observations and 75% by satellite systems.

Two issues of practicality known about the B-matrix are: it is ill conditioned and it is too large to represent explicitly. Ill conditioning increases the number of iterations for convergence, if convergence even remains a possibility, and can seriously degrade analysis quality, El-Said (2015). Even if convergence were to be achieved, for an ill-conditioned B, this would increase the likelihood of convergence on a non-unique (or nearly non-unique) local minimum, rendering the resulting analysis almost useless. The impossibility of storing B, implicitly dictates needing to build the action of the square-root of B, in the form of a series of coded procedures. These two problems are simultaneously and conveniently dealt with by a change of variable, known as the control variable (or vector) transform (CVT). CVT allows implicit B-matrix specification, avoiding B inversion, explicit memory storage. A surrogate control vector is thus introduced, which conveniently preconditions, de-correlates and greatly reduces it to a more manageable size.

Specification of a surrogate control vector requires knowledge of its structure (modeling B), and commensurate estimation of the parameters governing its structure (estimating B). The large body of research behind modeling the structure of B in the last two decades strongly suggests that B is: anisotropic, heterogeneous, multivariate and flow-dependent, Bannister (2008). The global ECMWF and Meteo-France weather models rely on expansion of the fields as spherical harmonics. The HARMONIE NWP system uses the ALADIN model, which is an adaptation of the global Meteo-France model for regional areas. ALADIN utilizes an extension zone to represent the fields as bi-periodic. A Fast Fourier Transform (FFT) technique is then used to calculate the bi-Fourier harmonics. The spatial correlation structure therefore follows a spectral convolution rendering spatial structures as isotropic and homogeneous. Spectral convolutions are also vertically nonseparable, meaning that broad horizontal correlations are deep, and narrower horizontal correlations are isometrically shallow in 3D space. Nonseparability facilitates correct, and necessary, specification of mass-wind correlations (Bartello & Mitchell, 1992; Phillips, 1986). Balance is incorporated by imposing locally linearized geostrophic and hydrostatic balances. Vorticity and geopotential are related via the f -plane assumption, which is appropriate for the ALADIN domain. The Coriolis and Laplacian operator ratio in the f -plane equation is estimated by linear regression, Berre (2000). Multiple linear regressions are then used to estimate divergence, temperature and surface pressure, and specific

humidity. This entire procedure comprises the balance operator. The extension to specific humidity was added to ALADIN, after adapting the original NCEP method (Derber & Bouttier, 1999; Parrish et al., 1997).

Estimating the B-matrix is of commensurate importance to modeling it. The statistical material provided to the B-matrix directly influences any given analysis. The three known methods for estimating the B-matrix are: the observation-background disentanglement technique, Hollingsworth and Lönnerberg (1986), the NMC method, Parrish and Derber (1992), and statistics obtained from forecast differences originating from an Ensemble of Data Assimilation (EDA) analyses, Fisher (2003). The EDA-technique enables time-varying background error if updated with sufficient temporal frequency. EDAs can also provide insight into model uncertainties, Palmer (2001). The EDA technique performs several analyses, usually at lower resolution, where each member is distinguished by a mixture of either; perturbing observations, SST fields, initial conditions, model physics, according to prescribed statistical distributions and thus covariance matrices. The subsequent analyses are then used to produce short forecasts and differences between these forecasts are computed to provide the statistical material needed for the B-matrix.

“Flow-dependence” is a particular aspect related to both B-matrix modeling and its estimation. The literature on B-matrix estimation uses flow-dependence to broadly pertain to interdependence of atmospheric variables on atmospheric or dynamical flow. The mathematical specification of flow-dependence translates to geostrophic and hydrostatic balance equations, both of which are a spatio-temporally evolving phenomenon. The literature often asserts flow-dependence, while the explicit temporal aspect of flow-dependence in mathematical terms is implicitly present, to varying degrees. For example, via a static B-matrix averaged over a specific time-frame. A particular example is an EDA of 3DVARs is used in Brousseau et al. (2012), where the balance operator in B is modeled by linearized analogs of the nonlinear balance equations (from Berre (2000)), and background errors are estimated via a temporally moving average of 3DVAR EDAs over a specified time-frame. This has a degree of flow-dependence, incorporating spatial balance structures evolved temporally. Flow-dependence in Bonavita et al. (2012) is achieved through the inherent time-propagation feature of 4DVAR in an EDA context, similar to ERA-Interim in a reanalysis context (Dee et al., 2011, described in Section 2.1.3). Another example from a similar time to the aforementioned studies, was done at the ECMWF outside the reanalysis context in Isaksen et al. (2007), where the balance operators are linearized around the background state, and a 10-member EDA of 4DVARs was used, without a moving average. In this paper, we ensure that all the forecast differences obtained from the EDA subjected to a temporal quotient using our new functionality, allowing the B-matrix to be estimated at frequent temporal intervals throughout. An advantage of incorporating temporal tethering in this way is alleviating the need to reconfigure the B-matrix during re-analysis production, which is useful given the time-span involved. The ERA-Interim report shows that the design consideration of B-matrix retuning, due to temporally changing observation networks over decadal time-frames, was not needed in a reanalysis context, Dee et al. (2011).

In this paper, we investigate the impact of varying the degree of influence placed on different sources of forecast differences arising from the CERRA-EDA system for computing a synchronous B-matrix at prescribed temporal intervals. We do this in the context of the CERRA reanalysis system, over the European and North-African domain, with a total time-span of ~40 years. The CERRA system, is described fully in Section 2, with brief details on the observations used in Section 2.1, and B-matrix design in Section 2.2. The potential statistical variability of background error relevant to CERRA is shown in Section 2.2.2, followed by details on the new forecast difference temporal quotient in Section 2.2.3. Section 3 details our line of enquiry, with a brief explanation of the weather regime paradigm used, and describes our proposed case study. We detail the design of the case study in Section 3.1, and how the actual CERRA-EDA system is used to investigate the bandwidth of possibilities offered by our method in Section 3.1. The highlights of our investigation with illustrative examples are discussed in Section 3.2. Finally, we conclude our main findings in Section 4.

2. The CERRA System

The CERRA system was developed to deliver the European regional reanalysis as described in the previous section, with a domain covering Europe, Northern Africa and South-Eastern parts of Greenland, as in Figure 2. A condensed picture of CERRA is pictorially illustrated in Figure 1. The CERRA system consists of two principal streams: the principal deterministic stream, CERRA-DET and an EDA stream, CERRA-EDA. Both of these

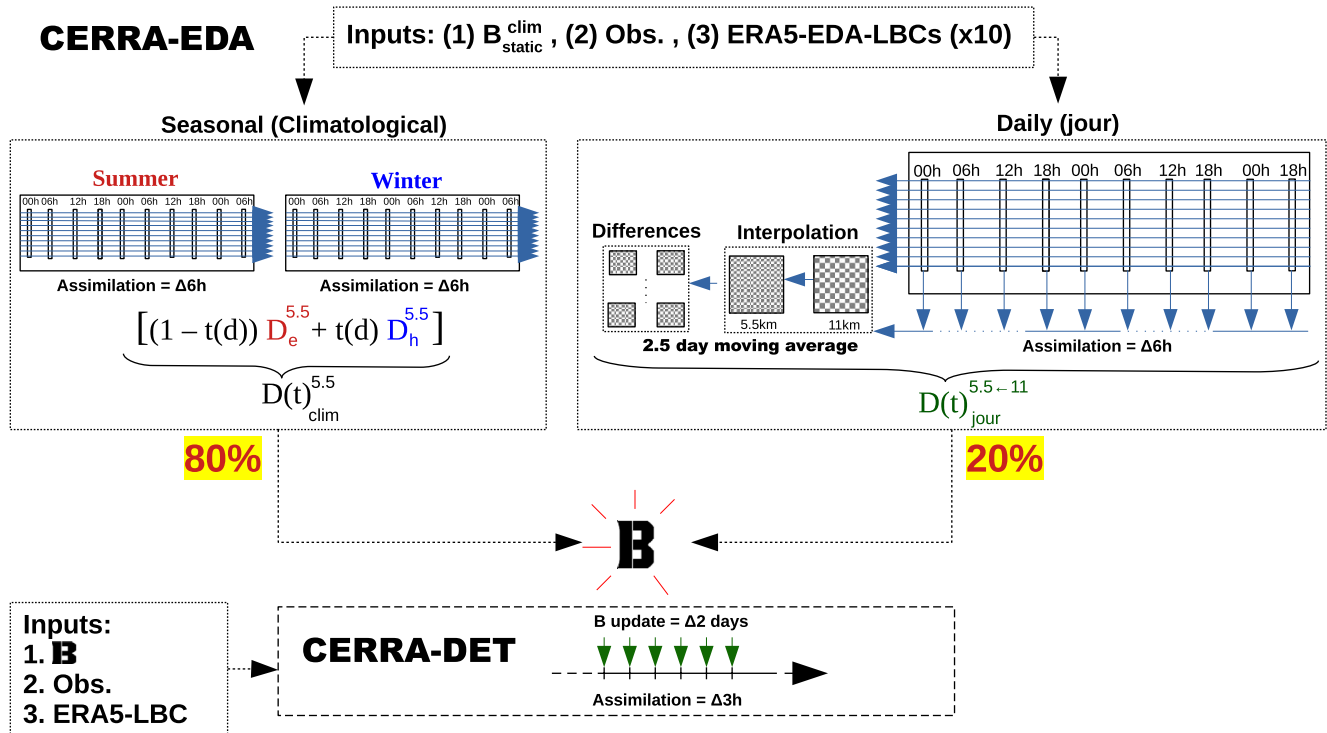


Figure 1. Condensed diagram of the Copernicus European Regional Re-Analysis (CERRA) system, which comprises CERRA-DET and CERRA-ensemble of data assimilations (EDA). B_{static}^{clim} denotes a CERRA-EDA-input climatological (50% summer 50% winter) B-matrix which is static. $D_{e/h}^{5.5}$ denotes forecast differences at 5.5 km arising from summer (e-ete) and winter (h-hiver) periods, whereas $D_{jour}^{5.5-11}$ denotes 11 km interpolated up to 5.5 km, for the (jour-daily) forecast differences. $t(d)$ is a time function dependent of day within given year. Equation references are explained further in Equation 8.

streams compose CERRA, and when we refer to just “CERRA” herein, it refers to both CERRA-DET and CERRA-EDA. CERRA uses the HARMONIE NWP system (code cycle version: cy40h1), with ALADIN physics, 3DVAR to analyze the upper atmosphere, and an Optimal Interpolation (OI) technique to analyze the surface. CERRA is set to 106 vertical levels. CERRA-DET has a horizontal grid-box resolution of 5.5 km, a 4-min time-step and assimilates eight times per day. CERRA-EDA is a 10-member Ensemble of 3DVAR Data Assimilations with 11 km grid-box resolution, 10-min time-step and assimilates four times a day.

ALADIN is coupled to an OI surface analysis system called MESCAN. MESCAN adopts its name from SMHI’s “MESoscale Surface analysis” (MESan), Häggmark et al. (2000), and Météo-France’s “Code d’Analyse Necessaire à ARPEGE pour ses Rejets et son Initialization” (CANARI) systems. MESCAN is coupled to ALADIN, and analyses 2-m temperature and relative humidity (T2m and RH2m, respectively). Once the T2m and RH2m increments are computed, MESCAN updates soil moisture, surface temperature and deep soil related variables using a relatively simple two-layer model. SURFEX simply stands for “SURFace EXternalisée,” an external 14-layer surface model, Masson et al. (2013), which will be run after the completion of CERRA, computing variables such as: run-off drainage, ground water charge, flood plains, water budget, evaporation fluxes, soil moisture and snow depth. This will be known as CERRA-Land.

CERRA-DET and CERRA-EDA are shown to have three inputs worth mentioning: B-matrix, observations and Lateral Boundary Conditions (LBCs). The two that differ are the B-matrix and the LBCs. CERRA-DET obtains its LBC-forcing from a 31 km resolution 31 km ERA5-LBC stream. The observations used are detailed in Section 2.1. The B-matrix it uses, is modeled as in Section 2.2, and estimated using CERRA-EDA, which is explained further in Section 2.2.3.

CERRA-EDA itself uses a static climatological B-matrix for each member when it minimizes each of its respective 3DVAR, with equal influence from both summer and winter periods (detailed further in Section 2.2.3, Equation 7). These are 6-hr forecast differences done at 5.5 km. ERA5’s dedicated EDA stream, providing 10 LBCs, which we make full use of in CERRA-EDA. Each ensemble member is obtained by perturbing the same

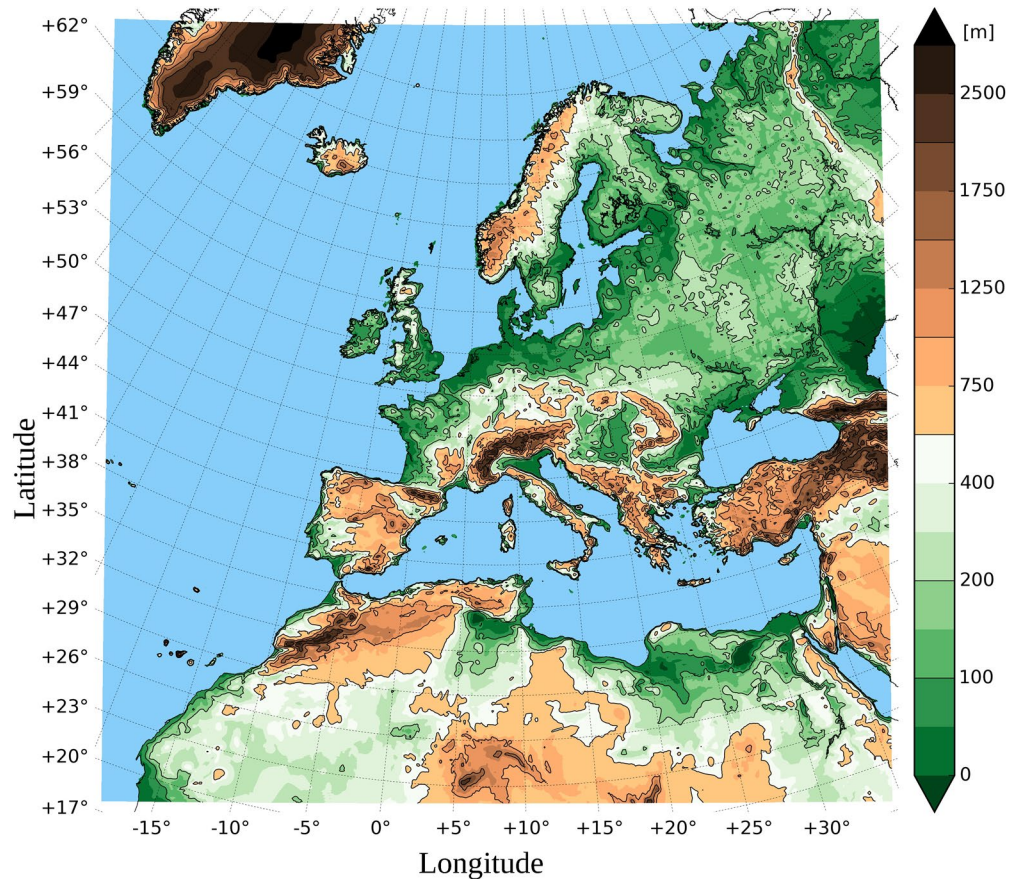


Figure 2. Copernicus European Regional Re-Analysis (CERRA) domain illustrated by model topography. Grid points having a water surface of at least 80% are shown in light blue.

set of observations, at each assimilation time for each member. The lateral boundary conditions (LBCs) come from ERA5. ERA5 similarly has a main stream, 31 km and 20-min time-step, with an accompanying 10-member EDA at 63 km and a 12-min time-step, Hersbach et al. (2020).

2.1. Observations

The observations used for CERRA are obtained from two main sources: the Meteorological Archival and Retrieval System (MARS) and European Center File Storage system (ECFS) at the ECMWF. These observations include conventional observations: synoptic surface observation stations (SYNOP), ships and drifting buoys. Other observations include: radiosonde, aircraft (AIREP, ACAR, AMDAR), satellite radiances from different instruments such as Advanced Microwave Sounding Units (AMSU-A and AMSU-B), Microwave Humidity Sounder (MHS) and Infrared Atmospheric Sounding Interferometer (IASI), and satellite based atmospheric motion vector (AMV) wind data. Ground-based observations of zenith total delay (ZTD) from the Global Navigation Satellite System (ground-based GNSS) are also used. The ground-based observations from GNSS are part of a network of reprocessed ZTD's provided by the European Reference Permanent Network (EUREF-EPN, Bruyninx et al. (2019)). Furthermore, GNSS-RO (Radio Occultation) observations provided by the Global Navigation satellite system receiver for Atmospheric Sounding, from EUMETSAT's large network of Satellite Application Facilities (GRAS-SAF) are also reprocessed to increase the signal to noise ratio. Finally, scatterometer observations are fetched directly from the EUMETSAT dissemination center EUMETCAST. In addition, we have excluded data from NOAA's older Microwave Sounding Unit (MSU) data, which had temporal coverage from 1978 to 2005, due to unresolved technical issues.

Table 1

Average Number of Observations for Each Assimilation Cycle (in Thousands) for the Whole Month of March in Each Respective Year as Used in Copernicus European Regional Re-Analysis (CERRA)

Year	1985	1991	1998	2003	2012	2018
Total	11.9	12.4	14.5	34.2	79.1	78.9
Satellite	1.0	0.8	0.7	10.6	40.6	38.3

Table 1 gives a broad picture of the temporal evolution of average number of observations throughout the majority of the CERRA time-frame. The temporal change in observation networks particularly in March is of interest to us, as our case study in Section 3 is in March. It is important to mention the temporal evolution of observation quantities due to differing observation networks, especially in the context of reanalysis, since it has been previously shown to be an important factor due to its potential impact on background error covariances and therefore the analysis (Brousseau et al., 2012).

Table 1 also shows the influence of satellite observations, particularly their dramatic increase at the turn of the century, making up roughly 25% up from nearly 5%. An illustration of increasing dependence on satellite observations is revealed by looking at ATOVS and IASI data. For example, in 2018 they could make up to 90% of the total observations at a single assimilation time, whereas on average this is largely not the case. Observation processing also increases as the number of observations increase, raw observations can be of the order 10^7 preprocessing, reducing by up to three orders of magnitude postprocessing, for any single assimilation time. These illustrative synoptic statements have been seen in the diagnostic output at a single minimization time during March 2018, but have not been explicitly shown here. Further details of the observations in CERRA are covered in Wang and Randriamampianina (2021). We now describe the design of the B-matrix.

2.2. B-Matrix Design

The B-matrix is not stored explicitly. However, we can elucidate each of its constituents to gain insight into its role in CERRA's 3DVAR. The spatial correlation matrix, containing one block for each total wave-number of the spectral model, for the correlations between the four control variables: wind (vorticity $[\xi]$ and unbalanced divergence $[\eta_u]$), the unbalanced mass field (temperature and surface pressure $(T, P_s)_u$) and unbalanced specific humidity (q_u) is such that:

$$\mathbf{C} = \begin{pmatrix} \mathbf{C}^\xi & & & \\ & \mathbf{C}^{\eta_u} & & \\ & & \mathbf{C}^{(T, P_s)_u} & \\ & & & \mathbf{C}^{q_u} \end{pmatrix}, \quad (1)$$

where $\mathbf{C} \in \mathbb{R}^{4NL \times 4NL}$. Each block contains vertical and horizontal correlations, for all total wave-numbers $n = 1, \dots, N$ and for all model levels $l = 1, \dots, L$, where $L = 106$. Note that vorticity is considered balanced. The structure of one of these blocks, specific humidity for example, has the form:

$$\mathbf{C}^{q_u} = \begin{pmatrix} \mathbf{h}_{(1)}^{q_u} \begin{pmatrix} v^1 v^1 & v^1 v^2 & \dots & v^1 v^L \\ v^2 v^1 & v^2 v^2 & & \vdots \\ \vdots & & \ddots & \\ v^L v^1 & v^L v^2 & \dots & v^L v^L \end{pmatrix}_{(1)} \mathbf{h}_{(1)}^{q_u} & & \\ & \ddots & \\ & & \mathbf{h}_{(N)}^{q_u} \begin{pmatrix} v^1 v^1 & v^1 v^2 & \dots & v^1 v^L \\ v^2 v^1 & v^2 v^2 & & \vdots \\ \vdots & & \ddots & \\ v^L v^1 & v^L v^2 & \dots & v^L v^L \end{pmatrix}_{(N)} \mathbf{h}_{(N)}^{q_u} \end{pmatrix}, \quad (2)$$

where $\mathbf{h}_{(n)}^{q_u} = \text{Diag}(h^1, \dots, h^L)_{(n)}^{q_u} \in \mathbb{R}^{L \times L}$, $\mathbf{V}_{(n)}^{q_u} \in \mathbb{R}^{L \times L}$ is the matrix in-between $\mathbf{h}_{(n)}^{q_u}$ in Equation 2, and $\mathbf{C}^{q_u} \in \mathbb{R}^{N \times N \times L}$. The subscripts (n) denote the total wave numbers. The super-scripted values inside each constituent block, h^l , v^l , denote the horizontal and vertical correlation values at level l , respectively.

The balance operator contains the multivariate balance relationships as originally devised by Derber and Bouttner (1999) and later adapted to ALADIN, Berre (2000), such that:

$$\mathbf{L} = \begin{pmatrix} \mathbf{I} \\ \mathbf{MH} & \mathbf{I} \\ \mathbf{NH} & \mathbf{P} & \mathbf{I} \\ \mathbf{QH} & \mathbf{R} & \mathbf{S} & \mathbf{I} \end{pmatrix}. \quad (3)$$

\mathbf{L} is the balance operator in spectral space. It accounts for the mass-wind and specific humidity balances, separate from the correlations dealt with in \mathbf{C} . The theoretical idea is that \mathbf{L} addresses hydrostatic and geostrophic balances in the vertical and horizontal by rendering the related variables as multiple linear regressions to be estimated. The vertical balances for mass-wind are taken into account by \mathbf{M} , \mathbf{N} , and \mathbf{P} and these are related to specific humidity via \mathbf{Q} , \mathbf{R} , and \mathbf{S} . The horizontal balances are applied with the horizontal balance operator \mathbf{H} , which is a diagonal matrix taking spectral vorticity coefficients and obtaining balanced geopotential by multiplication of the assumed linear regression coefficients. Balanced geopotential is the balanced part of the linearized mass variable deduced from (T, P_s) via the linearized hydrostatic relationship as in Parrish et al. (1997).

The final stage is to combine these steps to represent the total B-matrix such that:

$$\mathbf{B} = \mathbf{L}^T \mathbf{\Sigma}^T \mathbf{C} \mathbf{\Sigma} \mathbf{L}. \quad (4)$$

where $\mathbf{\Sigma}$ comprises σ_b along the diagonal, representing the background standard deviation for the respective wave-number, level and variable in spectral space. The regression coefficients, standard deviations and horizontal and vertical correlations are all updated every time the forecast differences are harvested from the EDA. This is described in the next section.

2.2.1. B-Matrix Estimation: CERRA-EDA

CERRA-EDA is used to estimate the B-matrix for CERRA-DET. It is also used as a proxy for uncertainty quantification in tangential applications to do with CERRA in general. CERRA-DET assimilates the observations, as described in Section 2.1, without perturbation. CERRA-EDA is a 10-member ensemble of assimilations, where each member is distinguished by having the same set of observations but perturbed using a diagonal observation

error covariance matrix with zero mean following a Gaussian distribution. Once each observation is perturbed, a 3DVAR assimilation is performed and an analysis follows.

Each 3DVAR is cyclicly performed every 6 hr. The analysis of each member is then used to produce a 6-hr forecast. These forecasts are forced by perturbed LBCs from the ERA5-EDA. This EDA implementation permits the consideration of observation error, implicit background error and implicit LBC error in the data assimilation process. Model error is not taken into account, as none of the conventional techniques such as Stochastic Perturbation of Physical Tendencies (SPPT) Stochastic Kinetic Energy Backscatter (SKEB) have been included.

The differences of these 6-hr forecasts are computed between each adjacent ensemble member such that:

$$\mathbf{d}_{i,i+1}^f = \mathbf{x}_i^{f6h} - \mathbf{x}_{i+1}^{f6h}, \quad (5)$$

for member i , such that $i = 0, \dots, 8$ and $\mathbf{d}_{9,0} = \mathbf{x}_9^{f6h} - \mathbf{x}_0^{f6h}$. These differences are then used to compute the correlations, multiple linear regression balance relationships, and standard deviations that compose the B-matrix. The differences between these background fields have the statistical characteristics of differences between fields of background errors. This means they have the covariance structure of background error, but twice the variance:

$$\sigma(\epsilon^f) = \frac{1}{\sqrt{2}} \sigma(\mathbf{d}^f), \quad (6)$$

which is also loosely known as the “residual NMC” value. Further explanations and schematics to how background error statistics are general from an ensemble in this way are elucidated in Fisher (2003).

The choice of 3DVAR, 10-members, 11 km and 10-min time-step, for the EDA were a sufficient compromise to meet constraints on computational expense and implementation. The effect of the number of EDA ensemble members on the behavior of background error standard deviations are discussed Section 3.2.1. Reducing the resolution from 5.5 to 11 km yields half the number of grid points in both directions of the bi-harmonics, and allows for an increase in time-step. This explains why CERRA-DET has a 4-min time-step in comparison to CERRA-EDA's 10-min time-step.

We have chosen this route of using an EDA with 3DVAR mainly as an optimal compromise to satisfy operational deadlines and resource constraints such as running cost, complexity (maintenance), and running time (speed). Another reason is that in the context of the reanalysis, reasonable measure of uncertainties that can be obtained from an EDA is required.

2.2.2. Potential Statistical Variability

Prior to developing CERRA-EDA a preliminary system was created and successfully tested on Météo-France's OLIVE-ALADIN system. We use the results from this system as an illustrative analogue in this section only, and in Figures 3–5. OLIVE is the bespoke scripting shell used at Météo-France to control their NWP systems. This acted as the blueprint for the ensuing CERRA-EDA system. It is this preliminary system that was used to identify potential variabilities requiring consideration and decisions with regards to developing CERRA-EDA. This section discusses plots produced using this preliminary system. The OLIVE-ALADIN EDA system had 5.5 km grid-box size, five-members and forced by 42 km LBCs from AEARP (Météo-France's global EDA system for ARPEGE), cycled 6-hourly with differences taken from 6-hr forecasts. The two periods used for the results shown in this section were 1st–18th July 2017 and 1st–18th December 2018.

The only differences between this preliminary system and the CERRA-EDA system are the number of members and LBC grid-box resolution. The difference in the number of members is discussed in our case study in Section 3.2.1. The difference in resolution of the LBCs between those provided by ARPEGE and ERA5 did cause a marked difference in the B-matrix statistics. This difference was systematic and arbitrary however. The overall variation profiles and behaviors remained the same. This is worth mentioning but is not shown in this article.

The potential areas of statistical variability relevant to our study here are: the model and its resolution, time-scales (daily, weekly, monthly, and seasonal), and the observation systems over decadal time-scales. These areas of variability have been investigated in the literature and are known, and they have also been echoed in Brousseau et al. (2011); Brousseau et al. (2012). Weather regime change can be categorized under daily variability. An illustration of the potential variability that can be exhibited day-to-day is shown in Figures 3 and 4.

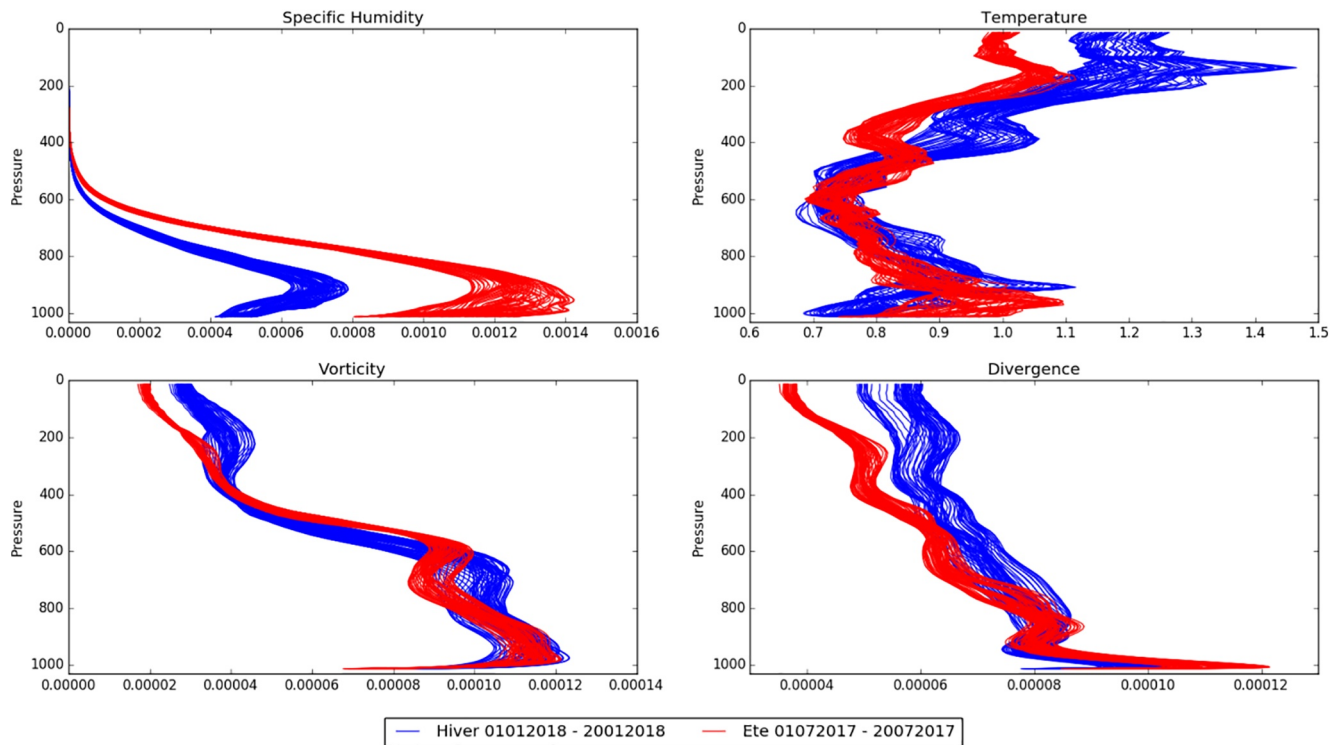


Figure 3. Vertical σ_b profiles as a function of pressure (hPa) for the following variables: specific humidity (top-left), temperature (top-right), vorticity (bottom-left) and divergence (bottom-right). Each profile represents σ_b for one assimilation time. Summer is represented by the period 1st–20th July 2017 (red lines), and winter 1st–20th December 2018 (blue lines).

Figures 3 and 4 both simultaneously show potential seasonal and daily variabilities. Figure 3 shows total σ_b values in the vertical, where between 1,000 hPa and 800 hPa there is potential of a 50% change in the base σ_b value for specific humidity from summer to winter for example. Similarly, the top-left plot in Figure 4 shows larger potential variability can be seen in the horizontal scales, where nearly an entire order of magnitude of change in specific humidity is possible for the largest scales ($\sim 10^3$) and the smaller scales ($\sim 10^2$).

Figure 5 shows the temporal variability of σ_b . In Figure 5a, the total σ_b^{Ps} value over time has potential to change significantly from the base value that would otherwise be predicted by a seasonally static set of statistics arising from a climatological B-matrix (dotted-lines).

An important parameter that we derive from the general theme exhibited by Figure 5, more specifically Figure 5d for vorticity, is that the steepest gradient in σ_b occurred from days 10 to 12 $\frac{1}{2}$ (approximately). This illustrates that the maximum change shown in this preliminary experiment for a control variable is 2 $\frac{1}{2}$ days. This contributed to our choice of using 2 $\frac{1}{2}$ -days-worth of assimilation times in length as a moving average, for CERRA-EDA. This is then used to update the B-matrix every 2 days in CERRA-DET, as is described in the next section.

2.2.3. Forecast Difference Mixing

There are two pools of forecast differences used to produce the B-matrix: a 5.5 km climatological part and a 11 km daily part. The climatological part is a mixture of summer and winter differences, $D_e^{5.5}$ and $D_h^{5.5}$, respectively, where subscripts “e” and “h” denote (ete-summer) and (hiver-winter), respectively. The forecast differences for $D_e^{5.5}$ and $D_h^{5.5}$ come from the following periods: 1st–10th July 2017 and 1st–10th January 2018 respectively (Figure 6). The forecast differences for these periods have been computed previously (offline) and are stored.

Conventionally the first climatological part comprises a fixed set of forecast differences, precomputed over a particular time period as in Brousseau et al. (2011). There is no time-varying mixture occurring. This is known as a static climatological B-matrix. We use this as our reference for the experiments in Section 3. Writing the forecast differences used for the static climatological B-matrix we have:

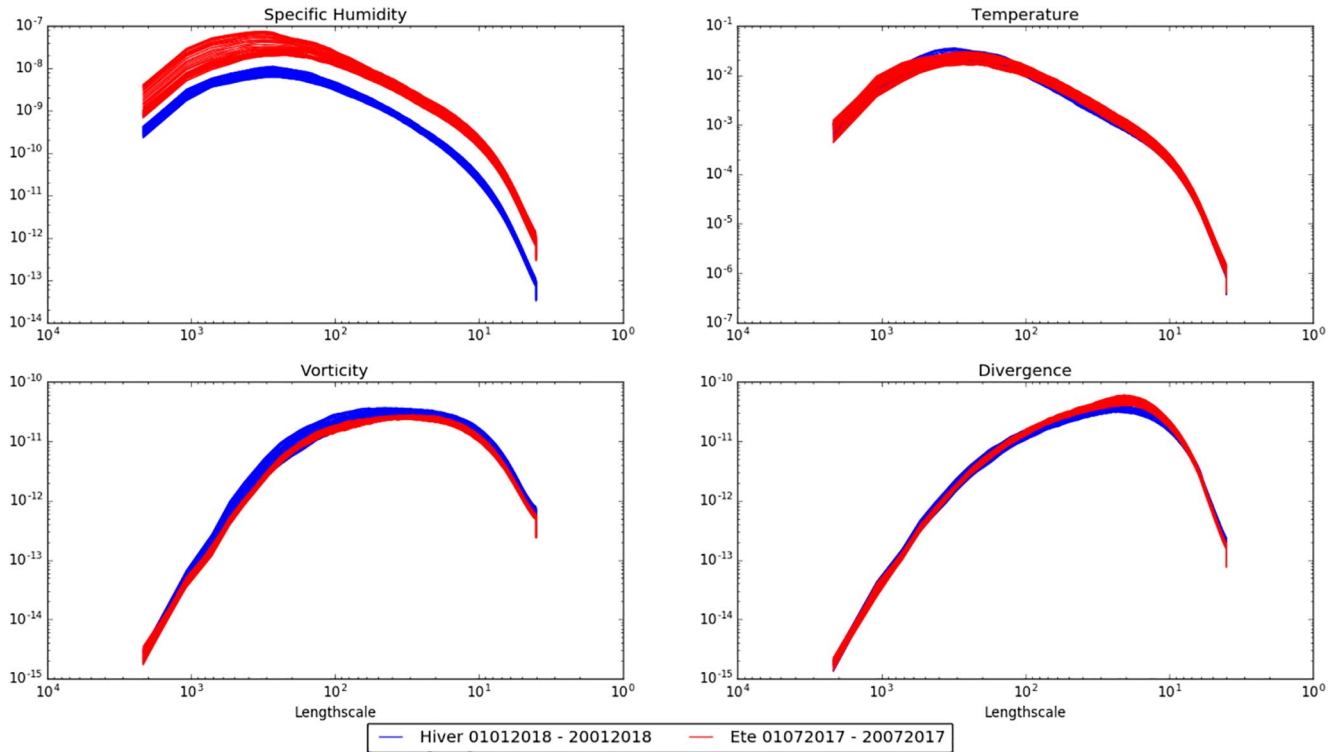


Figure 4. Horizontal σ_b^2 values as a function of length-scale (km) at ~1,000 hPa for the following variables: specific humidity (top-left), temperature (top-right), vorticity (bottom-left) and divergence (bottom-right). Each profile represents σ_b for one assimilation time. Summer is represented by the period 1st–20th July 2017 (red lines), and winter 1st–20th December 2018 (blue lines).

$$D_{clim}^{5.5} = D_e^{5.5}(1 - \tau) + \tau D_h^{5.5}, \quad (7)$$

where τ is an arbitrary constant. The differences composing $D_{clim}^{5.5}$ can generally have any resolution and come from any period, but we have written it this way to show the dual-seasonal split. CERRA-EDA itself uses the B-matrix described in Equation 7, which is different to the B-matrix derived from CERRA-EDA for CERRA-DET.

We take this one step further by introducing two-layers of time-dependency. A time-dependent function governing the proportion of summer and winter differences used, based on the time of year, synergizes an appropriate number of forecast differences from each season. This implies that $D_{clim}^{5.5}$ in Equation 7 will become time-dependent: $D(t)_{clim}^{5.5}$. Brousseau et al. (2012) employs a time-dependent version of $D(t)_{clim}^{5.5}$, cycling every 24 hr.

The second layer is also time-dependent, $D(d)_j^{5.5 \leftarrow 11}$, where “ j ” denotes jour and d is the current day in the year. The differences $D(d)_j^{5.5 \leftarrow 11}$ come from a lower resolution 11 km “online” CERRA-EDA running in parallel to CERRA-DET. Once the differences are taken at 11 km a standard quadratic interpolation technique is used to bring it up to 5.5 km.

The two-layer time-dependent function governing the proportion of forecast differences mixed to make the B-matrix is such that:

$$D(t)^{5.5} = \underbrace{[D_e^{5.5}(1 - t(r)) + D_h^{5.5}t(r)]}_{D(t)_{clim}^{5.5}} \alpha + (1 - \alpha)D(d)_j^{5.5 \leftarrow 11}, \quad (8)$$

where $D(t)^{5.5} \in \mathbb{R}^3$ is the total pool of forecast differences used to create the B-matrix at 5.5 km and α is the forecast difference mix ratio. For CERRA production, $\alpha = 0.8$. Notice that Equation 7 is a special case of Equation 8, where $t = \tau$ is fixed for all time, and $\alpha = 1$. t is a time-dependent periodic function, $t(r + T) = t(r)$, such that:

$$t(r) = \frac{r(d)}{h}, \quad (9)$$

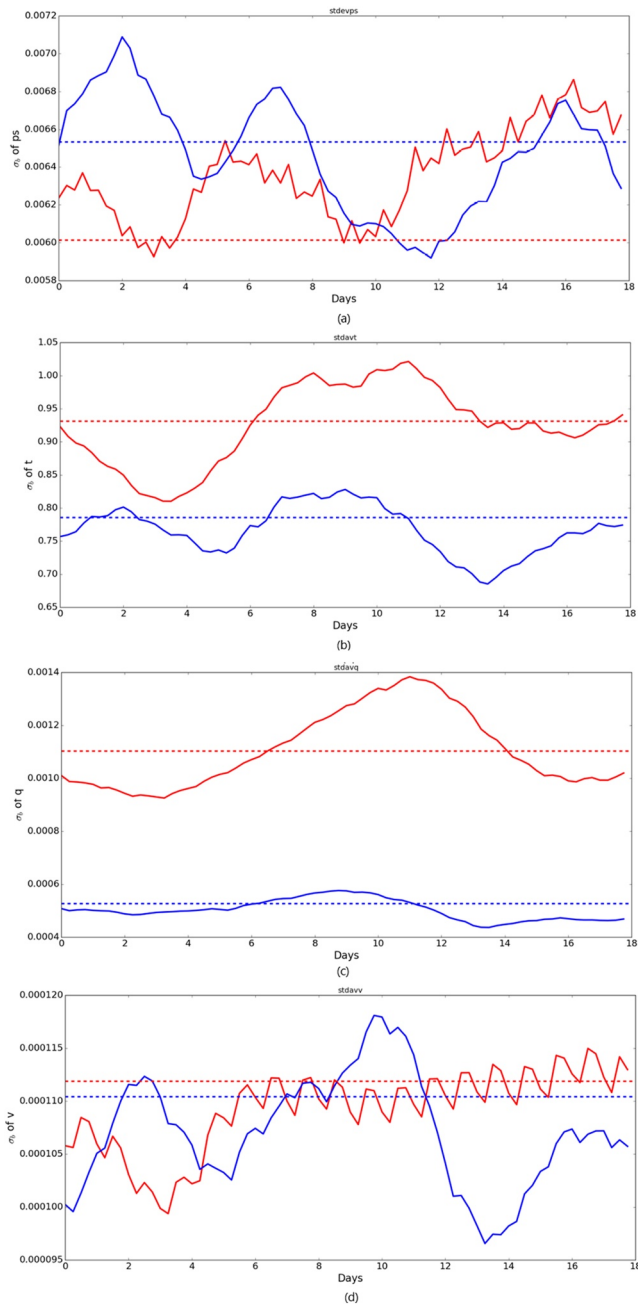


Figure 5. Total σ_b values for (a) surface pressure, (b) temperature, (c) specific humidity and (d) vorticity as a function of days in the month. Each line represents the total σ_b value for each day in the respective month of the experiment. First 18 days of December 2018 (blue-lines) and first 18 days of July 2017 (red-lines). The dotted lines are the σ_b values taken from the static climatological B-matrix, summer seasonal average (red-dotted line), and winter seasonal average (blue-dotted line).

where t depends on $r(d)$ such that:

$$r(d) = \begin{cases} -d \bmod h & \text{for } d \leq h \\ d \bmod h & \text{for } d > h \end{cases} \quad (10)$$

We set $h = 182$ to roughly represent half the days in the year. The period is roughly the number of the days in the year, $T = 365$ as is the current day in the year, represented by $d \in [1, 365]$. For example, $d = 1$ would imply that the date is 1st January and $d = 365$ is 31st December. The forecast differences, $D(d)_j^{5.5-11}$, constitute $2\frac{1}{2}$ -day worth of assimilation times, as a moving average. This is to account for the maximum gradient of $\sim 2\frac{1}{2}$ -days seen in the preliminary studies we did prior to implementing CERRA, shown in Section 2.2.2, Figure 5.

Here is an example to illustrate how Equation 8 works. On the 1st January at 00:00 UTC say, we would have $d = 1$, $r(1) = 182$ and then $t(r) = 1$. Therefore, all the differences for $D(1)_j^{5.5}$ would come from $D_h^{5.5}$ and none from $D_e^{5.5}$. Finally, $D(1)_j^{5.5-11}$ would constitute a moving average of 2.5 days prior to and including the current hour, so everything from 18:00 29th December to 1st January at 00:00 UTC. At the very start of the cycle when these days are not available for $D(1)_j^{5.5-11}$, only 1st January at 00:00 UTC would be used. This means the CERRA 80%/20% quotient is cannot be strictly enforced temporarily. The moving average would incorporate the new days as it rolls forward in time, until it has the full 2.5 days on 3rd January 06:00, where the quotient becomes satisfied.

The purpose of the high-resolution EDA is to capture seasonal variability, and to estimate background error covariances for CERRA-DET's 5.5 km horizontal scales. This is the most important consideration in the context of our high-resolution regional reanalysis, hence the choice of $\alpha = 0.8$ was chosen for CERRA production. The purpose of the lower-resolution EDA is to have live tethering to the current meteorological situation, as is realized on a daily basis, for horizontal scales higher than 11 km. This has the potential to allow for changes arising from larger meteorological phenomena such as weather regime change.

3. Case Study: Can CERRA-EDA Capture a Change in Weather Regime?

We begin by asking the question: Can the way we introduce flow-dependency into our B-matrix sufficiently detect a change in weather regime? If so, are there any caveats? And, what impact does this have on the overall data assimilation system, and analysis and forecast quality? Before answering these questions we briefly explain how a weather regime is characterized.

There are numerous methods used to identify weather regimes. The data we use utilizes the methodology detailed in Vautard (1990). The way the authors compute the weather regime is by using a 24-hr centered finite difference of principal components of large-scale tendencies to compute instantaneous tendencies. A composite tendency function is the least squares cost function

of: small-scale tendencies, large-scale tendencies and other factors. The solution of this composite tendency function identifies the weather regime. Roughly speaking, an ensemble average of these composite tendency functions is taken, to ensure that the solutions (weather regimes) arrived at are statistically convergent. In this way, four weather regimes categorically emerge: a European blocking dipole, enhanced zonal flow, a positive anomaly over

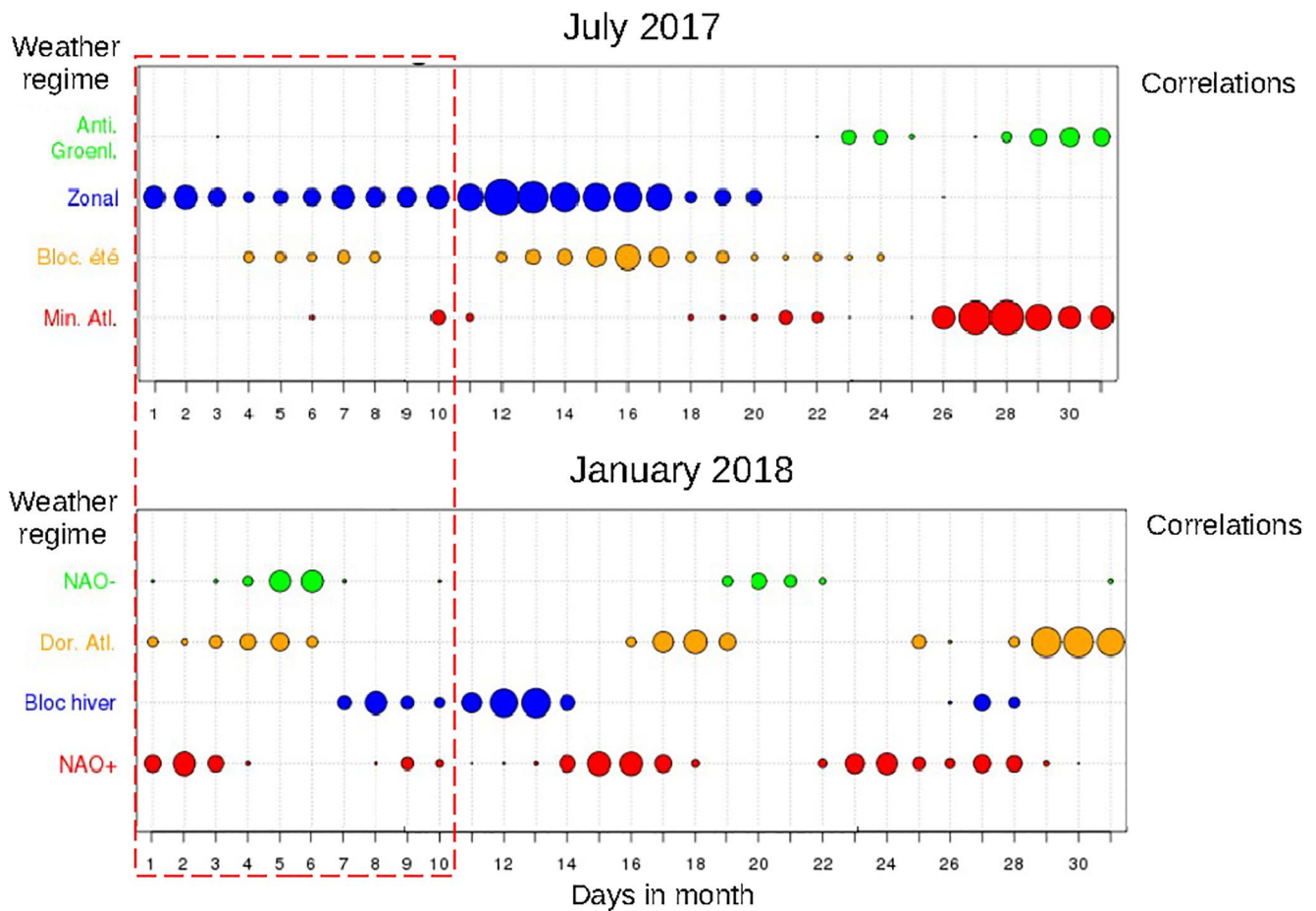


Figure 6. Weather regimes of periods used for $D(t)^{5.5}_{clim}$ climatological differences (ref: <http://seasonal.meteo.fr/content/suivi-clim-regimes-quot>). The summer period represented by the chosen days in July 2017 is dominated by a zonal regime, whereas the winter period represented by January 2018 shows a near-half between NAO+/NAO− followed by a less-imposing winter blocking regime. Weather regimes: Bloc. été/hiver, summer/winter blocking; Dor. Atl., Atlantic Ridge; Min. Atl., Atlantic Minimum; and Anti Groenl., Greenland Anti-cyclone.

Greenland and a ridge over the eastern Atlantic Ocean. Weather regimes in Europe are generally identified by quasi-stationary centers of pressure ratios at ~500 hPa roughly over the Azores Islands, west Portugal and Iceland. The weather regime paradigm is used to characterize large-scale circulation patterns over regional domains. It is also used as a proxy to predict significant short-to-mid-term changes in the statistical probability of hot and cold extremes and precipitation occurrences across Europe. We will term categorizations of weather regimes in Europe, as mentioned previously, as: North-Atlantic Oscillation (NAO +/−), Atlantic Ridge (Dor. and Min. Atl.), Blocking (bloc été/hiver), Zonal, and Greenland anomaly (Anti. Groenl, ref: Figure 6).

To be able to clearly identify if the B-matrix is capable of detecting a change in weather regime, we selected two periods where the winter regimes differ and exhibit clear changes of weather regime within the respective periods: March 2003 and March 2018, as shown in Figures 10 and 11.

3.1. Experiment Design

The underlying system used for experiments is CERRA, however, we vary α to obtain the different flavors of B. CERRA uses $\alpha = 0.8$ and this does not change. To produce the different B-matrices used in our experiments, we alter the α component in Equation 8. The static climatological B-matrix is composed as described in Section 2.2.3 Equation 7.

We seek to establish whether the ability of the B-matrix to recognize a change in weather regime is contingent on:

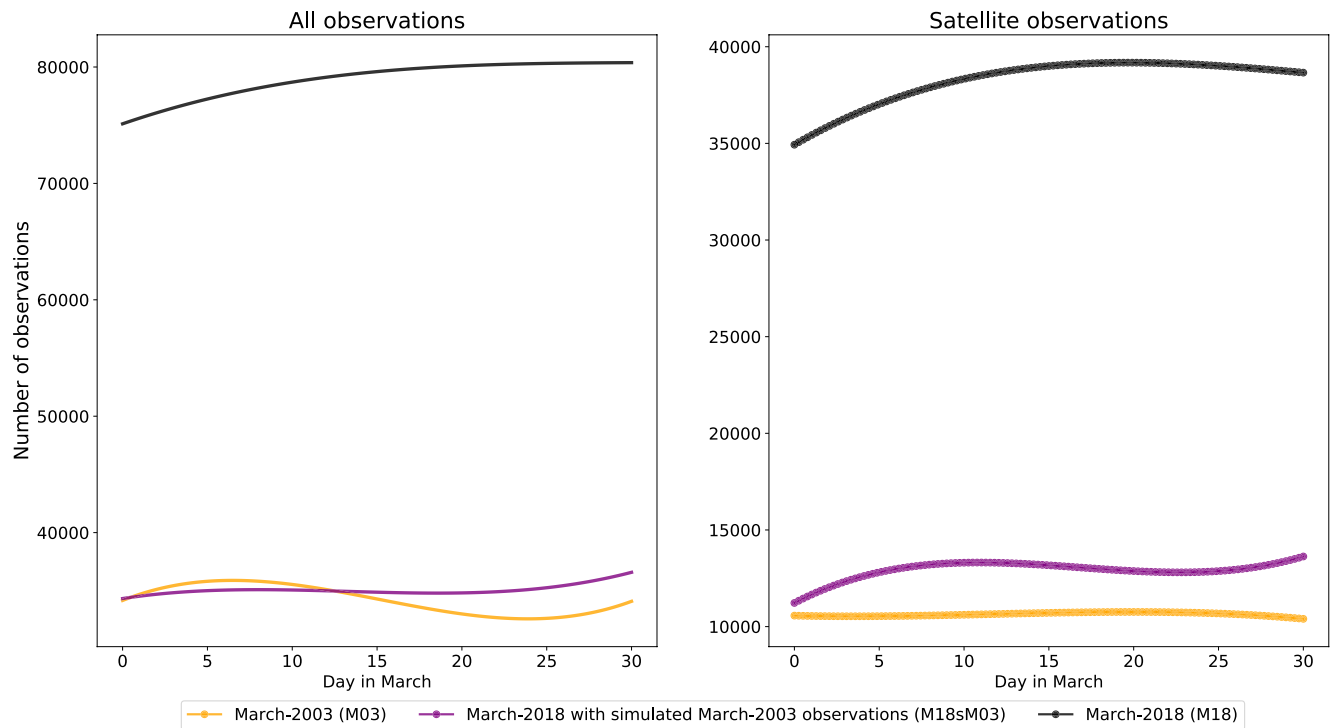


Figure 7. Averaged total numbers of observations (left plot) and satellite observations (right plot), by day in March (x-axis), for: March 2003 (orange line), March 2018 simulating March 2003 observations and March 2018 with default settings (black line). The observation data was averaged by being fitted to a 4th degree polynomial.

1. Varying climatology and daily forecast difference influence via α .
2. The observation network used in both respective periods.

To investigate varying the influence of climatology and daily differences, we compute the following B-matrices:

1. **BS** Climatology only. No daily. Equation 7 with $\tau = 0.5$.
2. **B8020** Climatology-dominant with daily. Equation 8 with $\alpha = 0.8$.
3. **B5050** Climatology and daily equal. Equation 8 with $\alpha = 0.5$.
4. **B2080** Daily-dominant with climatology. Equation 8 with $\alpha = 0.2$.

Additionally, we refer to the dynamic B-matrices, **B8020**, **B5050**, and **B2080** in the collective as **Bdyn**. To investigate the contribution of the observation network to the statistics we produce the B-matrices above using CERRA-EDA, and then run them with CERRA-DET, to produce analyses for the following periods:

1. March 2018 with default observation settings (M18).
2. March 2018 with observations settings closely mimicking March 2003 (M18sM03).
3. March 2003 with default observation settings (M03).

The abbreviations are used to refer to each period herein. M18sM03 allows us to isolate the general contribution of the observation network to the ensuing results. To allow the observation network of M18 to mimic M03 as closely as possible (M18sM03), we removed the following observations: SATOB (polar and geostrophic), Atmospheric Motion Vectors (AMV), Aircraft observations (AMDAR, AIREP, ACARS), and IASI. Figure 7 shows the averaged total and satellite observation numbers for M18, M18sM03, and M03.

Figure 8 illustrates the potential difference in spatial coverage at a single assimilation time shows significant aircraft coverage over the regions, which close to pressure centers and flow-corridors. This is sufficient reason to believe that this contributes to the enhanced ability of weather regime detection of M18 over M03. It is important to note that these aircraft observations were removed for the M18sM03 experiment. It is also important to note

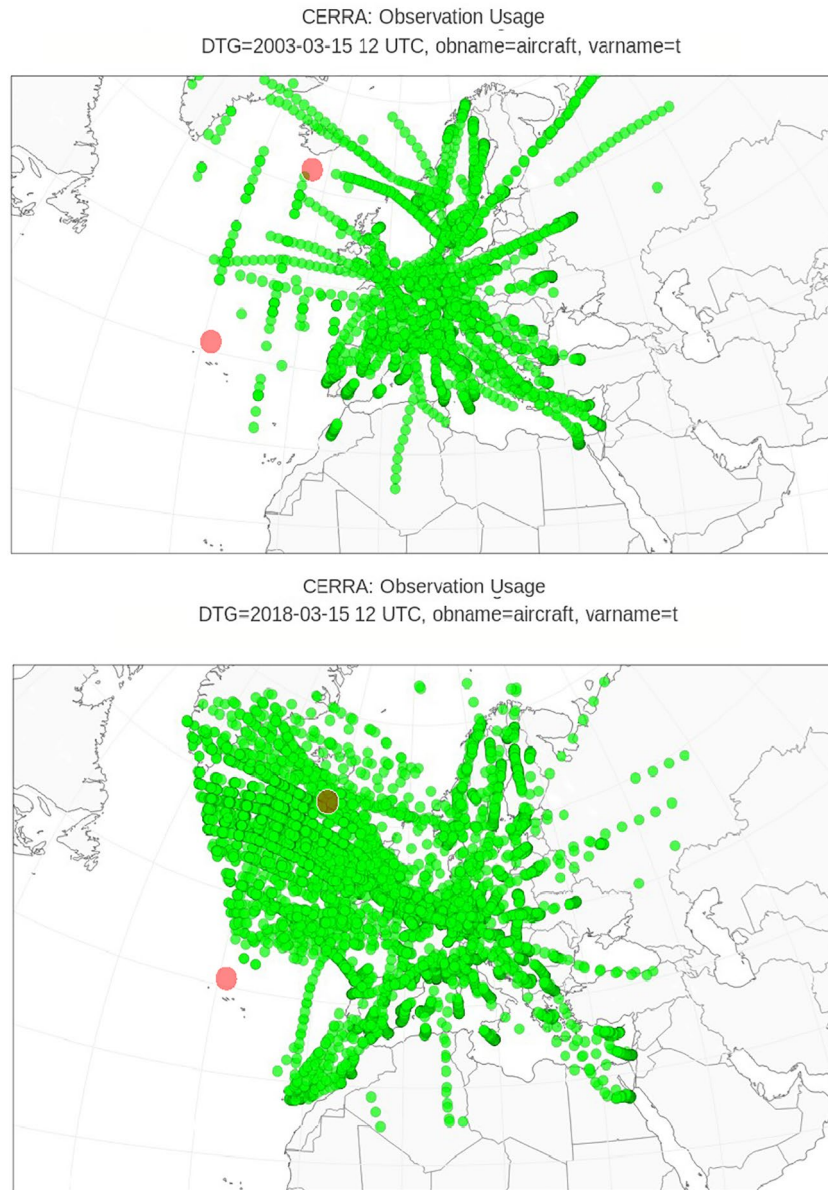


Figure 8. Aircraft observations over all vertical levels (green dots), with rough positions of North-Atlantic Oscillation (NAO) pressure centers: Azores Islands and South Iceland (red dots). The observations in each plot are a single assimilation-time snapshot for 15th March 2003 at 12:00:00 UTC (top plot) and 15th March 2018 at 12:00:00 UTC (bottom plot).

the marked difference in coverage densities illustrated by Figure 8. Figure 8 is a snapshot of the bigger picture illustrated in Figure 7.

It has also been shown in Wang and Randriamampianina (2021) that the aircraft observations had the most impact on CERRA analyses, which is relevant to us here since these form a part of the observations we removed for M18sM03.

3.2. Results

In this section we describe our results in four parts. The impact of each B-matrix on: the temporal evolution of σ_b , the spatial structures of σ_b , a single-observation experiment showing the horizontal and vertical cross-correlation structures, and the overall impact on the quality of the analysis and forecast.

The results are obtained by using B-matrices as described in Section 3.1. The observations used for the analysis in this entire section are the same as the assimilated observations in the experiment and in CERRA production.

3.2.1. Temporal Impact on σ_b

Figure 9 shows the behavior of the background error standard deviations with time, when using CERRA-EDA with 5 members (green-lines) and 10 members (red-lines). The behavior is very similar, showing the 5 member ensemble's timely and sufficient reaction to weather regime, while producing σ_b values that are systematically slightly less than the 10-member equivalent. However, the behavior of both EDAs is largely the same. This means that the statistical spread of σ_b decreases when using fewer ensemble members in CERRA-EDA. The maximum number of LBCs available from ERA5 was 10 members, and therefore we could not increase the number of members used any further.

The time series plots, shown as the bottom two plots of Figures 10 and 11, indicate two interesting aspects. The mean range of M18 (red lines) is quite narrow in comparison to M18sM03 and M03, showing a tendency to remain reasonably close to the σ_b value of BS, except in times of weather regime change. M18sM03 and M03 have comparatively wide σ_b ranges to M18, remaining virtually flat even in times of WR change. Since M18sM03 has a wide range of σ_b values, almost mimicking M03, it is fair to say that the large σ_b range is attributed to the difference in observation network, since M18 naturally has the improved observation network.

The second aspect is the flexibility of σ_b for M18, with the improved observation network. M18 is the only period showing any significant change at times of weather regime change. The α also plays a role here, since the changes are clearly more visible for $\alpha = 0.2, 0.5$. For example, M18 σ_b^q values (bottom plot: Figure 10) exhibit more readiness to change, while remaining close to BS's $\sigma_b^q = 4.8$ value. Another strong σ_b fluctuation between days 23 and 27 further illustrates the potential for rapid change, given a more weighty influence on the daily EDA statistics for B2080. This is mimicked in a more dilute sense for B5050. M03 and M18sM03 show near-to-no change in comparison to M18, except between days 26 and 28, and even then, it is very small.

It is therefore fair to conclude from Figures 10 and 11 that the coverage of the improved observations of M18 over M03, aid in the flexibility of σ_b at times of weather regime change, and the range of the σ_b values of each respective period. In aid of this conclusion, we see that both M03 and M18sM03 have nearly identical σ_b value-ranges and σ_b temporal flatness. This is due to having almost identical observation networks. It is important to factor in that aircraft observations were removed to allow M18sM03 to mimic the March-2003 observation network, which can be seen to provide vital coverage over areas characterizing weather regime change (Figure 8). For M18, it is both clear that σ_b is more willing to change and α facilitates the breadth of change σ_b can exhibit. This illustrates both the potentiality of the EDA to adjust to sudden changes in the meteorological situation, given sufficient observations, and the need to estimate α correctly.

3.2.2. Spatial Impact on σ_b

The horizontal profiles in Figure 12 illustrate the primacy of having a more effective and denser observation network for M18. Comparing M18 (blue lines) with M18sM03 (green lines), the blue line consistently has a higher variance profile across all wavelengths above 11 km. This is explained by half of the differences ($\alpha = 0.5$) coming from $D_j^{5.5-11}$. M18sM03 otherwise behaves almost identically to the bulk of the M03 profiles (red lines), where the few M03 profiles higher than M18sM03, particularly in the lower wave-length range for vorticity and divergence, is due to the different weather regimes present. These M03 profiles represent day 27 (as shown in Figure 11) where there is a slight increase in geopotential. M18 for those days is mainly NAO- with better observations and even higher geopotential values than M03, which explains the consistently higher vorticity and divergence profiles in the bottom two plots of Figure 12 for M18 over M03.

The vertical profiles in Figure 13 clearly show that increasing α , increases all standard deviation values for temperature throughout the vertical, regardless of period. Conversely, having the minimum value of $\alpha = 0.2$ as seen in Figure 13, the standard deviation of temperature is reduced by up to 1/3 of its original value.

Finally, comparing M18 to M18sM03 (left and middle plots, Figure 13), we observe that the range of σ_b^T values, within each respective B-matrix (B5050, blue lines and B2080, red lines), is much wider for M18. This is mainly due to the improved general observation coverage of M18 over M03 (Figure 7), allowing the change in α to have more effect. This is most visible for example, for $\alpha = 0.2$, where for M18sM03 (Figure 13, middle plot, red lines),

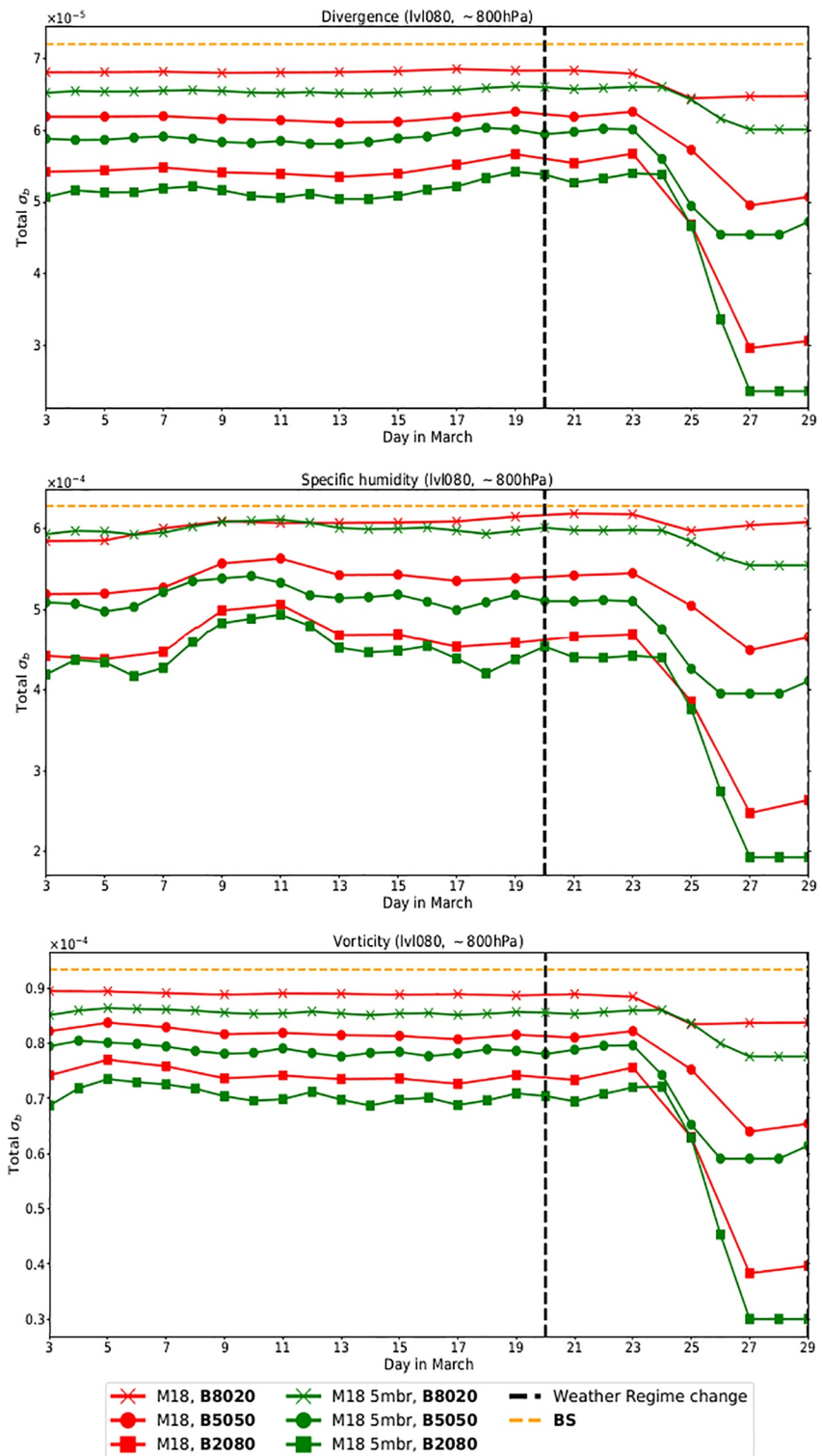


Figure 9. Total σ_b value at ~ 800 hPa for: divergence (top-plot), vorticity (middle-plot) and specific humidity (bottom-plot), for period 3rd–29th March 2018, for experiments with B-matrices: **B8020** (crosses), **B5050** (dots), **B2080** (squares), and **BS** (yellow-dotted-line). Additionally, CERRA-EDA with 5-members (green lines) and 10-members (red-lines). The vertical black lines divide periods of weather regime change.

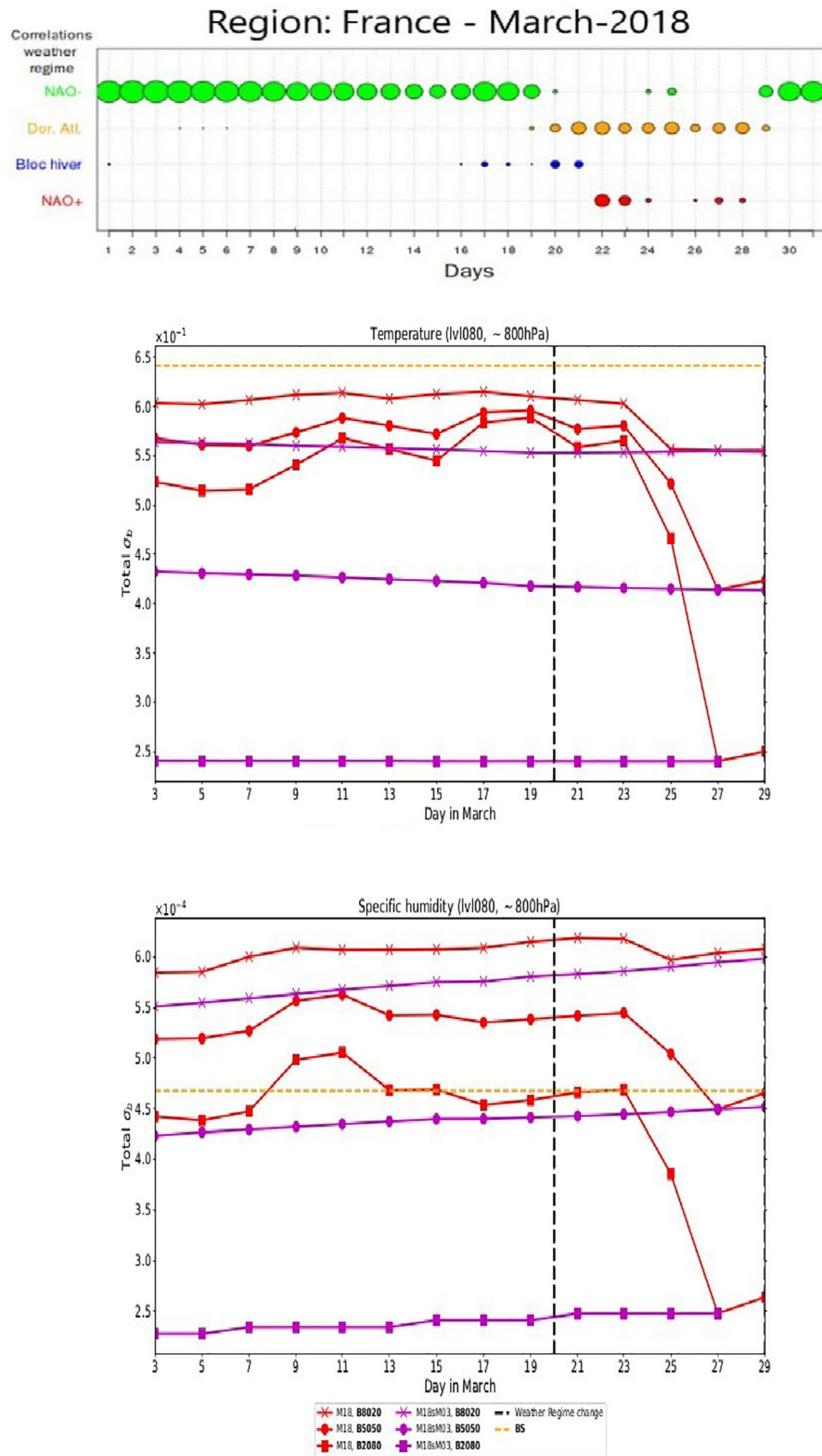


Figure 10. Top plot: actual weather regime correlations exhibited in March-2018 over France, with source and weather regime abbreviations as in Figure 6. Middle-plot: Total σ_b value for specific humidity at ~800 hPa. Bottom-plot: same as middle-plot but for temperature. M18 (red lines) and M18sM03 (purple-lines) with B-matrices: **B8020** (crosses), **B5050** (dots), **B2080** (squares) and **BS** (yellow-dotted line). The vertical black lines divide periods of weather regime. Period of middle and bottom plots: 3rd–29th March 2018.

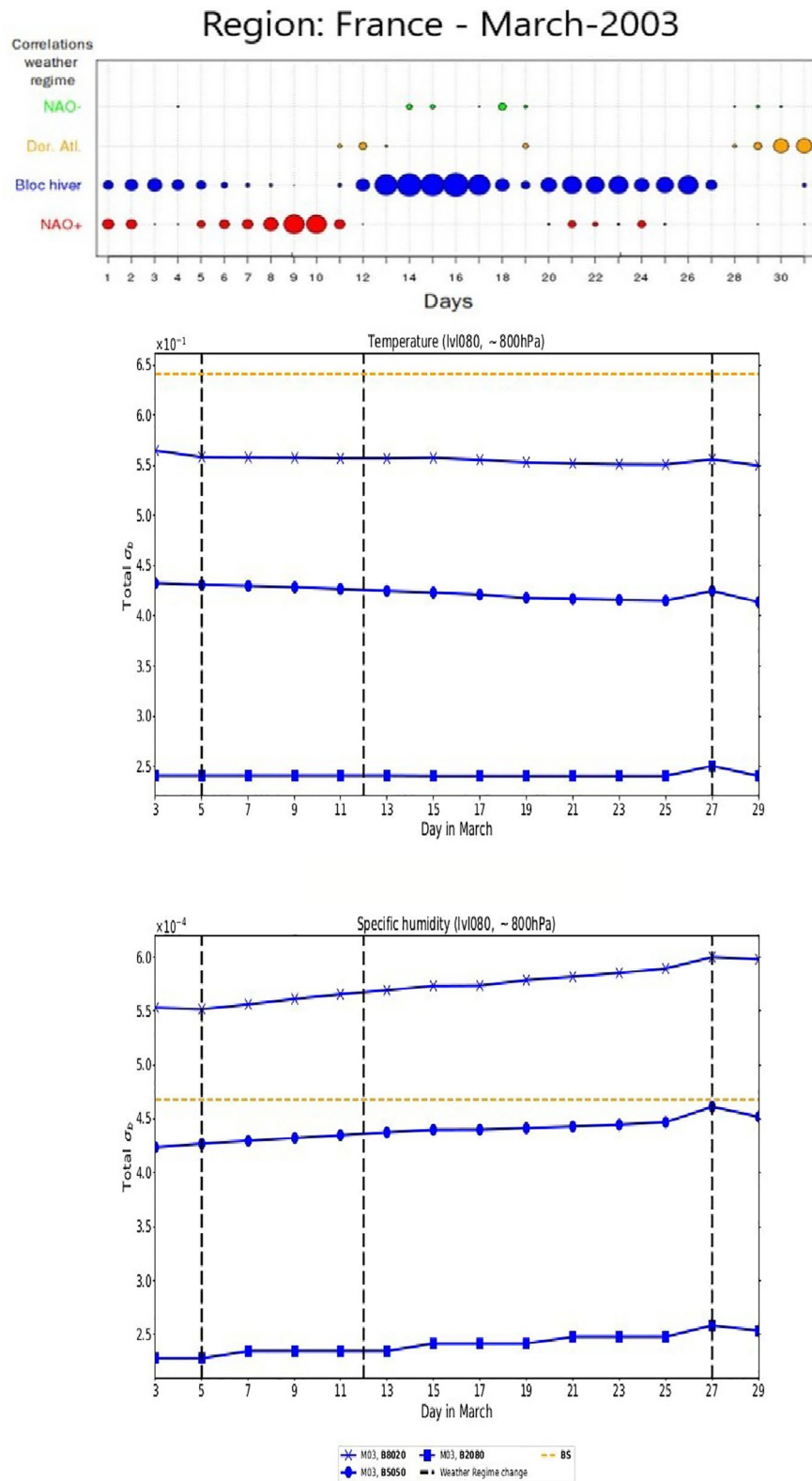


Figure 11. Top plot: actual weather regime correlations exhibited in March-2003 over France (ref: <http://seasonal.meteo.fr/content/suivi-clim-regimes-quot>). Middle-plot: Total σ_b value for specific humidity at ~800 hPa. Bottom-plot: same as middle-plot but for temperature. M03 (blue-lines) with B-matrices: **B8020** (crosses), **B5050** (dots), **B2080** (squares), and **BS** (yellow-dotted-line). The vertical black lines show period of weather regime change. Period of middle and bottom plots: 3rd–29th March 2003.

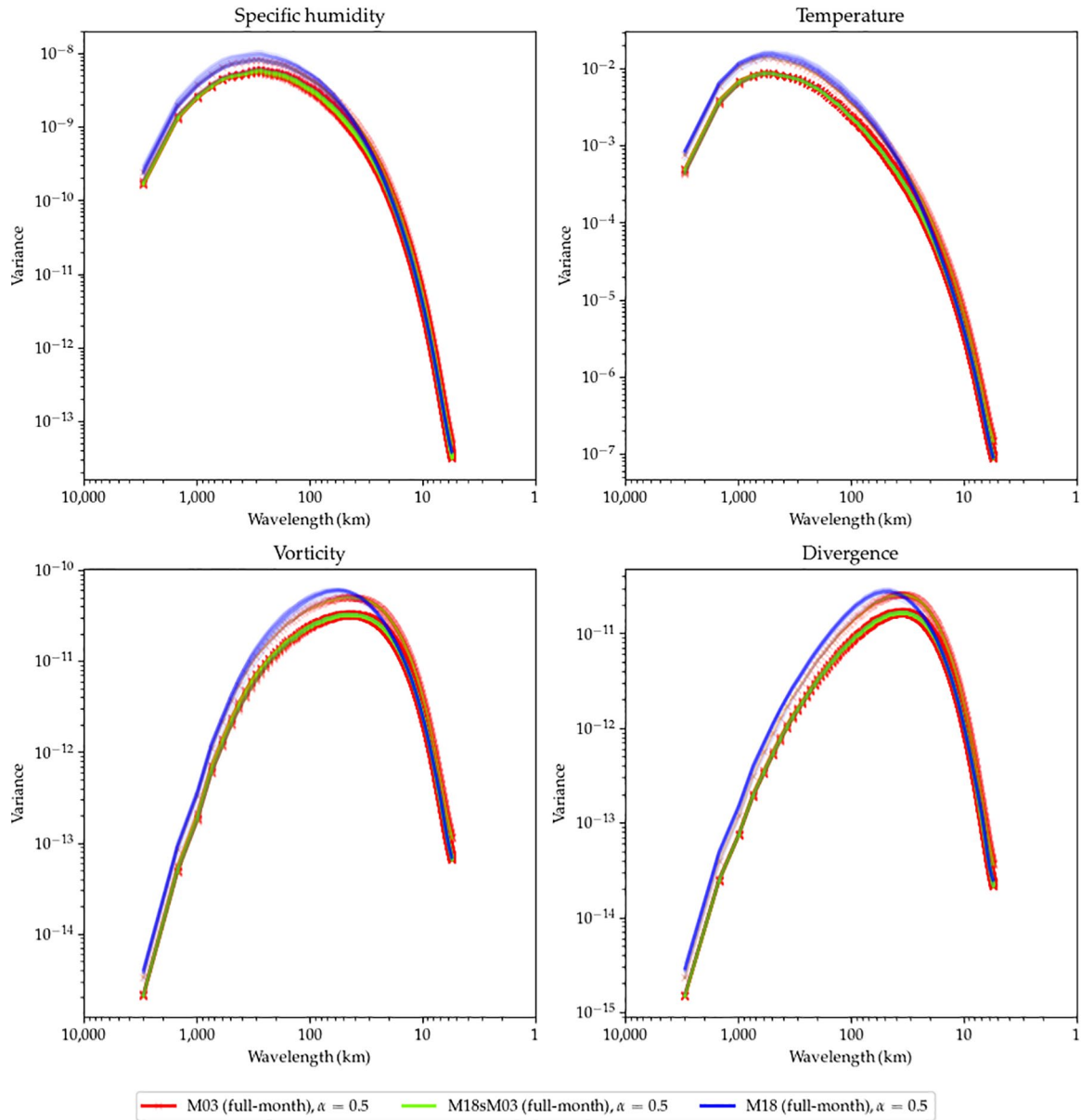


Figure 12. Horizontal σ_b^2 profiles at 1000 hPa of: specific humidity (top-left), temperature (top-right), vorticity (bottom-left) and divergence (bottom-right) for **B5050** ($\alpha = 0.5$) for experiments: M18 (blue lines), M18sM03 (teal lines) and M03 (red lines).

σ_b^T does not exceed ~ 0.4 , whereas σ_b^T in M18 can reach ~ 0.75 , similar to σ_b of **BS**, which has no daily influence. This illustrates the dynamic potential of the B-matrix with more daily-EDA influence than climatological with more observations by varying α . This also shows in the total σ_b value, Figure 10.

3.2.3. Single-Observation Analysis Increment Impact

Single-observation diagnostics are used here to illustrate the effect of the covariance structure, and differences between different matrices on the analysis increment. A single radiosonde observation of temperature at ~ 800 hPa (2.5 E, 45°N), corresponding to a max innovation of 3 K. This was done for the March 2018 (M18) only.

Figure 14 shows the effect of different B-matrices: **BS**, **B8020**, and **B5050**, on temperature (left side, plots a, c, and e) and specific humidity (right side, plots b, d, and f). It is clear that the most severe increment is attributed to **BS**, both in its size (a maximum innovation of 3 K) and in the surface area, it inhabits horizontally. The vertical

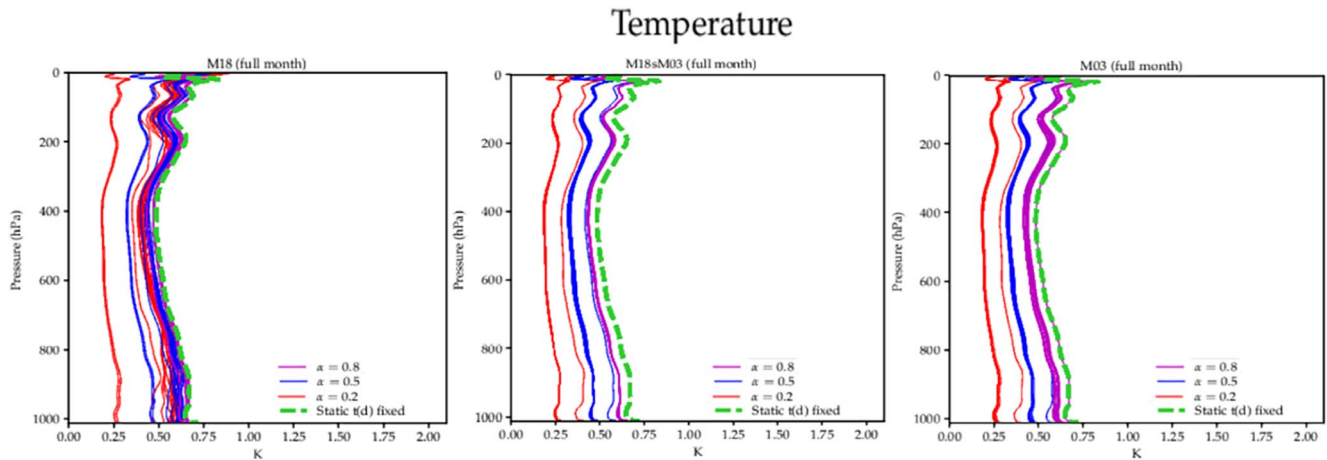


Figure 13. Vertical horizontally averaged σ_b profiles of temperature for the whole month of March: M18 (left plot), M18sM03 (middle plot) and M03 (right plot), respectively, for B-matrices: **BS** (green-dotted-line), **B8020** ($\alpha = 0.8$, purple lines), **B5050** ($\alpha = 0.5$, blue-lines), and **B2080** ($\alpha = 0.2$, red-lines). Each line represents the vertical temperature profile for one specific assimilation time.

cross-sections show that the differences in analysis increment area is very small between **Bdyn**, while the size of the increment is still slightly larger for **BS**.

Vertical and horizontal cross-sections for the **B2080** B-matrix of temperature, specific humidity and wind increments are plotted in Figure 15. The left-plots (a), (c), and (e) show the cross-correlation structures between the aforementioned variables during the NAO- phase of March-2018 (11th March), with the right-plots (b), (d), and (f) showing the much weaker increments during the Atlantic Ridge phase of March 2018. The decrease in increment severity seen in Figure 15 reflects the timely drop in σ_b since in Figure 10. The marriage of what is seen here in Figures 15 and 10 illustrates the correct capture of weather regime change. During an Atlantic Ridge, the increment is a lot smaller for temperature, specific humidity and wind, since the high pressure-center would block the North Atlantic jet-stream, which is amplified in the opposite situation of an NAO- regime. This is the desired outcome, to mirror reality more appropriately.

In summary, **Bdyn** exhibit lighter increments than **BS**, reflecting enhanced statistical awareness of weather regime change. This is reflected by using a time where there was a weather regime change versus not. The observation qualities are the same between all the matrices, however, **Bdyn** clearly adjusts to the weather regime change and **BS** does not. This shows that our method offers this advantage over a static B-matrix.

3.2.4. Evaluating Diagnostics, Analysis, and Forecast Impact

We begin by contrasting the results from Table 2 with Figures 10 and 11. The temporal behavior of wind background standard deviation is identical to temperature, and is therefore not shown. Anytime σ_b is mentioned, the reader is referred to Figures 11 and 10.

Table 2 shows diagnostics of relative difference of analysis and background departure root mean squares (RMSs) normalized by **BS** values. The diagnostics were done to show the whole period of March against the time in March where the weather regime change was most pronounced. The observation for the diagnostics are regularly distributed in space and time: aircraft measurements of temperature and wind, and ground-based GNSS for specific humidity. Relative differences of RMSs for background and analysis departures are referred to as RDRMS(O-B) and RDRMS(O-A), respectively. The RDRMS for a given experiment using B-matrix **Bdyn** is computed in the following way:

$$RDRMS = \left(\frac{RMS(\mathbf{Bdyn}) - RMS(\mathbf{BS})}{RMS(\mathbf{BS})} \right) \%. \quad (11)$$

To begin, we briefly explain how to interpret values in Table 2. For RDRMS(O-B) **B8020** values for example, these values measure how far the background-state produced by **B8020** actually is from the observations, in comparison to the **BS** equivalent, averaged over the period indicated. The same is analogously true for analysis

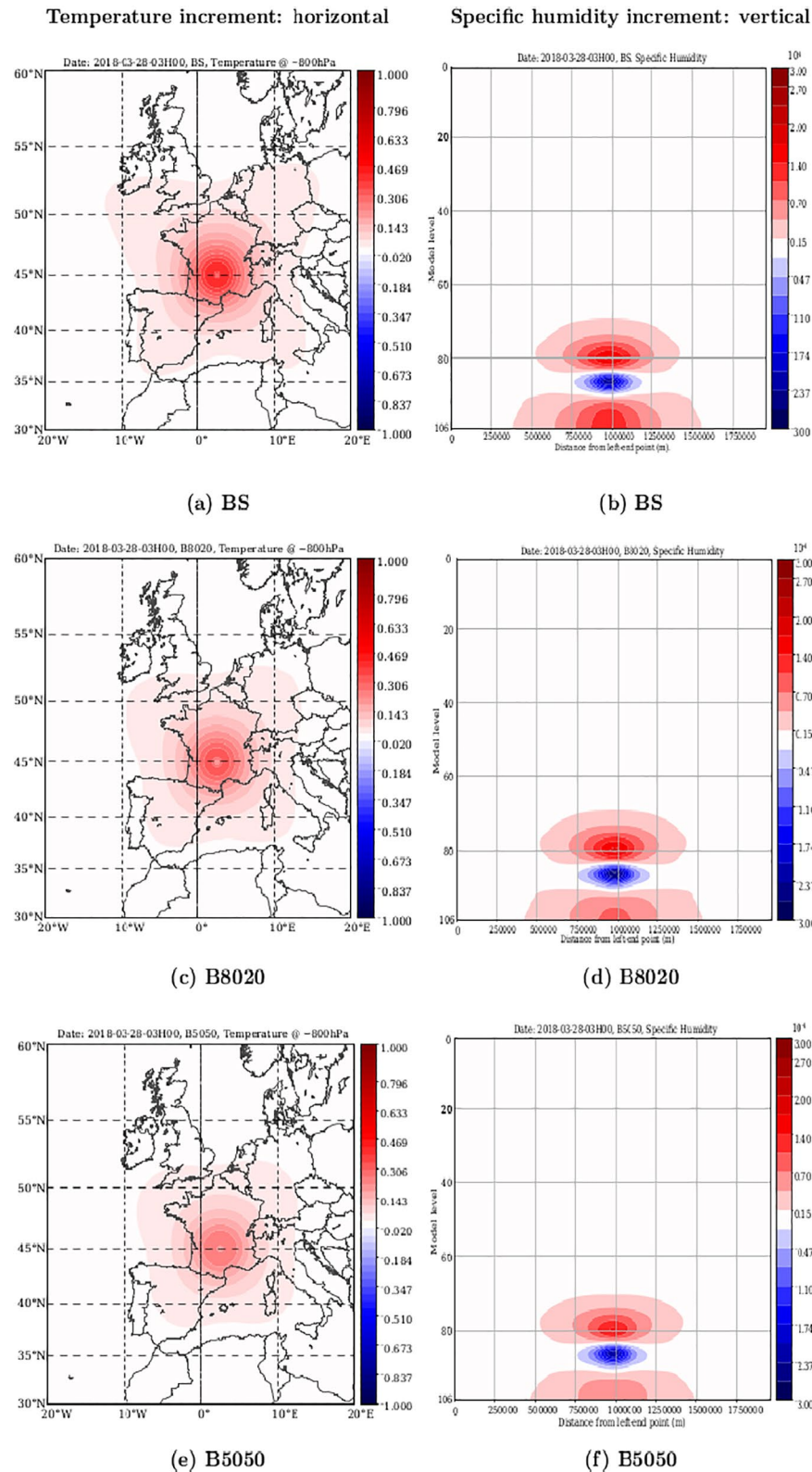


Figure 14. Analysis increments using a single radiosonde temperature observation at (2.5°E, 45°N), ~800 hPa, with an innovation value of 3 K. The left-hand side plots are the temperature analysis increments for the B-matrices: **BS**, **B8020**, and **B5050**, in longitude and latitude. The right-hand side plots are the specific humidity analysis increments for the B-matrices: **BS**, **B8020**, and **B5050**, against 106 vertical model levels and geometric latitudinal distance over the same geographical area as the left-hand plots (20°W–20°E, 30°N–60°N).

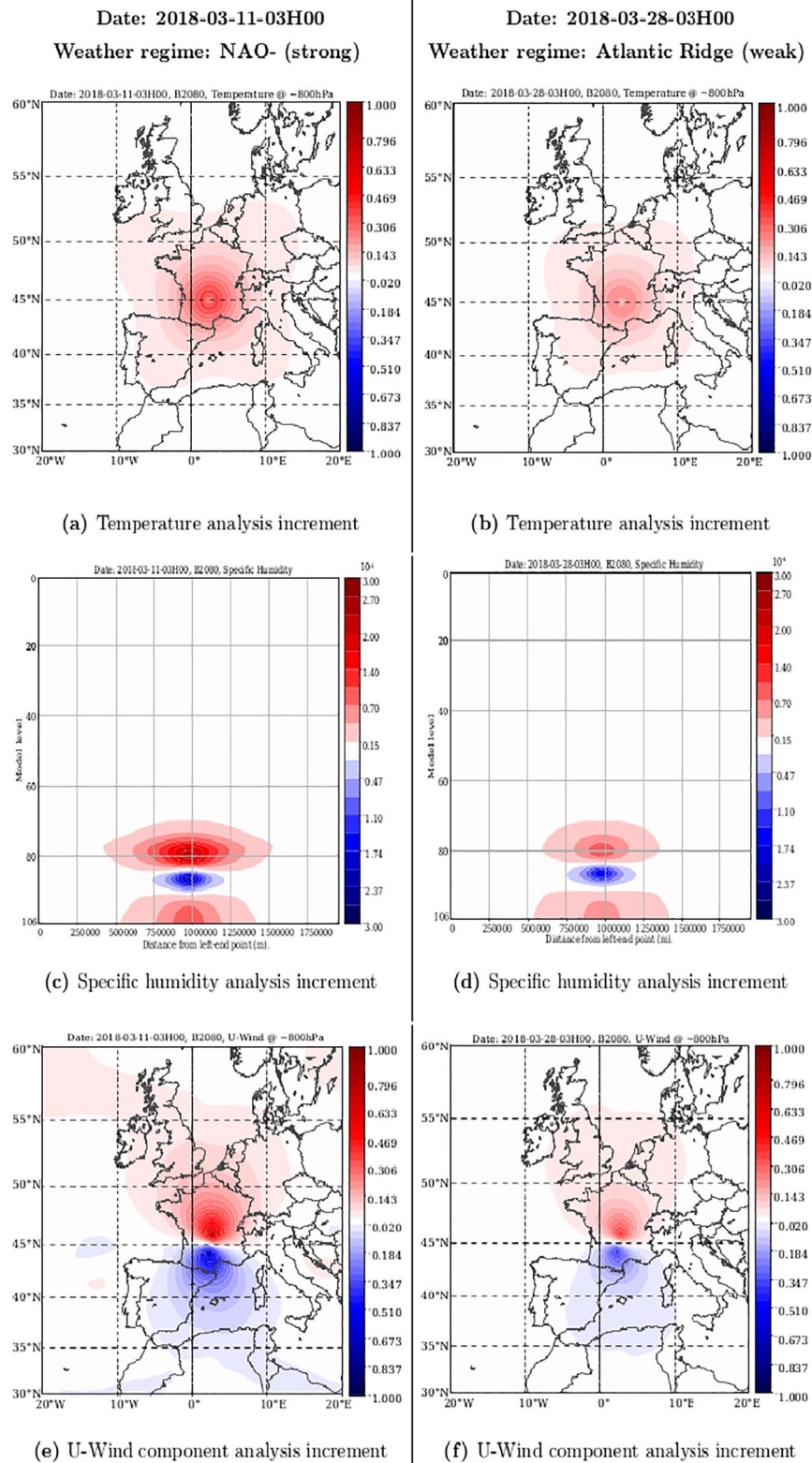


Figure 15. B2080 analysis increments using a single radiosonde temperature observation at (2.5°E, 45°N), ~800 hPa, with an innovation value of 3 K. These are for the same background and observation but with a different B-matrix. Left-hand side plots show longitude-latitude plots of: temperature (a), specific humidity (c) and u-wind component (e) cross correlations for 2018-03-11-03H00, with weather regime: NAO-. Right-hand side plots show the exactly the same variables (b), (d), and (f), for 2018-03-28-03H00 with weather regime: Atlantic Ridge (Dor. Alt.).

Table 2

Percentage Relative Differences of Root Mean Square (RMS) Values of Observation-Analysis (O-A) and Observation-Background (O-B) in the Observation Space for Aircraft Measurements of Wind, Temperature, and Ground-Based Global Navigation Satellite System (GNSS) Observations

B-matrix	Period	Wind ^a		Temperature ^a		Specific Humidity ^b	
		O-A	O-B	O-A	O-B	O-A	O-B
B8020	1–31st	4.1	–0.5	3.6	0.3	–8.9	–0.3
	26–31st	6.0	–1.2	5.0	0.2	–10.0	–1.5
B5050	1–31st	6.2	–0.7	6.1	0.5	–2.8	–0.5
	26–31st	12.0	–2.1	11.0	0.1	–1.1	–2.4
B2080	1–31st	7.0	–0.3	7.2	0.3	0.2	0.2
	26–31st	7.1	–0.2	6.8	0.2	–10.1	–1.7

Note. Each row shows B-matrices: **B8020**, **B5050**, and **B2080** compared to and normalized by **BS** during two distinct periods: 3–31st March 2018, and 26–31st March 2018. Positive values in rows for each period indicate that the RMS for the respective B-matrix is larger than **BS**. Bold number indicates statistically significant differences using a Student's *t*-test with 95% confidence interval.

^aAircraft observations. ^bGround-based Global Navigation Satellite System (GNSS).

departures, RDRMS(O-A). Positive values show how much the respective dynamic matrix has caused the analysis to move away from the observations in comparison to **BS**.

The σ_b value of temperature (and wind) is smaller for all dynamic matrices than the **BS** equivalent, implying that the daily-EDA induces more trust in the background compared to **BS**. This causes the positive RDRMS(O-A) values of temperature and wind (first column of Wind and Temperature, Table 2), indicating an analysis farther from the observations. Conversely, for specific humidity, σ_b values are more than **BS** equivalent (except for $\alpha = 0.2$), which show that the dynamic matrices are causing less trust in the background. As a result, the analysis fits the observations more closely (first column of Specific Humidity, Table 2). Figures 10 and 11 show σ_b values for temperature (and wind) are lower in the dynamic matrices compared to **BS**.

The (O-B) values show that changes seen in wind and specific humidity benefit the subsequent background in the assimilation cycle. Therefore RMS (O-B) values are slightly reduced with the lowest reduction being 0.3% for specific humidity in **B8020** and the highest being 0.7% for wind in **B5050** for the whole period of march over **BS**. However only the **B8020 B5050** reductions in RDRMS (O-B) values are statistically significant. The opposite is true for temperature where the RMS (O-B) values increase slightly, but the changes are mostly not statistically significant.

The period of weather regime change shows the most significant change of σ_b values for the dynamic B-matrices compared to **BS**. These changes are seen in the reduction of RMS (O-B) values (second columns and second rows for wind and specific humidity, Table 2) with a maximum reduction of 2.4% for Ground-based GNSS observations in **B5050**. This significant change between these two periods is not true for **B2080** however. **B2080** shows RMS values for (O-A) and (O-B) for wind and specific humidity variables (second row of **B8020** and second row of **B8020**, Table) that are close to **B2080** values. This indicates that increasing the proportion of daily information from the EDA has no added benefit in this case. A plausible reason for this is the disparity between the resolutions of the daily (11 km) and seasonal (5.5 km) forecast differences. The additional information from the daily differences is only relevant for model scales above 11 km.

We have shown that the use of dynamical B-matrices using our method offers more potential to improve the general behavior of this cyclic data assimilation system. This is relevant to the CERRA resolution and general reanalysis context.

The impact of dynamic B-matrix changes on the quality of the forecasts during the data assimilation cycle are further evaluated using precipitation skill scores shown in Figure 16. The 24-hr accumulated precipitation is simulated by the sum of eight 3-hr forecasts from the data assimilation cycles between 6 UTC and 6 UTC the following day, and compared to rain-gauge measurements. There are ~4,850 rain-gauge measurements available each day. Figure 16 shows the relative difference of Hiedke Skill Score (HSS) for measured precipitation thresholds every

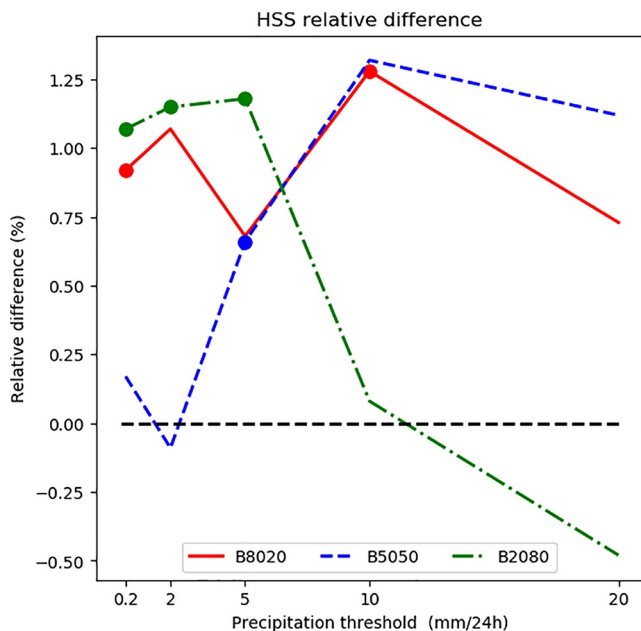


Figure 16. Relative differences of Hiedke Skill Scores (HSS) for 24 hr accumulated precipitation measurement thresholds (mm). HSS is compared to the chance score. The differences for each threshold are between measurements by rain gauges (4,850 on the geographical domain) and the sum of the 3-hr range forecasts from the data assimilation cycle (background) between 06 UTC and 06 UTC the next day. This is for the period from 01 to 31 March 2018. The zero-value is marked by (dashed black-line), **B8020** (solid red-line), **B5050** (dashed blue-line), and **B2080** (dash-dot green-line). Each experiment is compared to and normalized by **BS** for 0.2, 2, 5, and 10 mm/24hr thresholds. Circles on lines indicate statistically significant differences using a Boot-strap test with 95% confidence interval.

24 hr (0.2, 2, 5, and 10 mm/24hr) for **B8020**, **B5050**, and **B2080** experiments compared to **BS**. Positive values indicate that the dynamic B-matrix experiment is closer to the observations than **BS**. Circles on the curves indicate that the differences are statistically significant.

B8020 exhibits slightly better HSS values than **BS** (positive values, HSS is higher in **B8020** than **BS**) for all the thresholds around the 1% relative difference region. However, this improvement is significant only for 0.2 and 10 mm thresholds. **B5050** only shows a significant improvement for the 5 mm threshold, while **B2080** is significantly better for 0.2, 2, and 5 mm thresholds. For other thresholds the HSS differences are not significant.

Our choice of **B8020** for CERRA seems to be the best compromise when viewed in light of Table 2 and Figure 16. The quality of cyclic analyses and cyclic background qualities shown in Table 2 are similar for **B8020** and **B5050**, both of which perform better than **B2080** in this regard. Also, when viewing Figure 16 alone, **B8020** performs better than **B5050**, but not as well as **B2080** for low precipitation thresholds, and **B2080** is worst for higher rainfalls. The sure-footed choice therefore is **B8020** since it is the most constrained in terms of the amount of information it permits from the 11km-scales, in comparison to **B5050** and **B2080**.

While one of the main purposes of a reanalysis system is to provide optimal estimation of the atmosphere state at a given time, the system can also be used to initialize longer-range forecasts for operational NWP. To examine this potential and the aptitude of the system to provide input data for longer range forecasts, Figure 17 shows normalized RMSE of the analysis, 12-hr and 24-hr forecasts all valid at 00H00 and 12H00 UTC, of geopotential and temperature fields using radiosonde measurements. Each of these forecasts arises from using the dynamic B-matrices against forecasts using **BS** as our benchmark comparator. So positive values (right-side of 0, Figure 17) indicate improved forecast quality of the respective dynamic B-matrix over **BS**.

As previously discussed, the smaller σ_b values of dynamic B-matrices for temperature and wind compared to **BS** result in subsequent analyses which fit the observations less, that is, the background is more trusted. As Table 2 generally shows larger increments to RDRMS(O-A). March 2003 shows differences between the dynamic B-matrices and **BS** which are not significantly different from zero. Conversely, during March 2018 these forecast ranges exhibit statistically significant improvements (positive normalized RMSE differences) for the 600–300 hPa layer, indicating that the changes in the data assimilation system benefit the forecast quality in that region. Dynamic B-matrix σ_b values have the potential to increase over **BS**, providing analyses closer to observations and also better subsequent forecast as a consequence. However, it is difficult to see any clear improvement in analysis or forecast skill quality in the temperature and geopotential fields seen in Figure 17. This was also the case for the specific humidity field, which have been omitted as it does not add any new insight.

The HSS precipitation skill scores were shown to be statistically significant, showing improvement of the dynamic B-matrices built with our method over **BS**. However, the forecast skill scores remain largely similar to **BS** and thus inconclusive.

4. Conclusions

In this paper, we introduced a new temporal quotient on the use of EDA forecast differences used to estimate the B-matrix for CERRA. The CERRA-EDA system was designed specifically for use in CERRA, a regional 5.5 km ~40-year reanalysis. CERRA production had a 80%–20% seasonal-daily split with its B-matrix updated every 2 days.

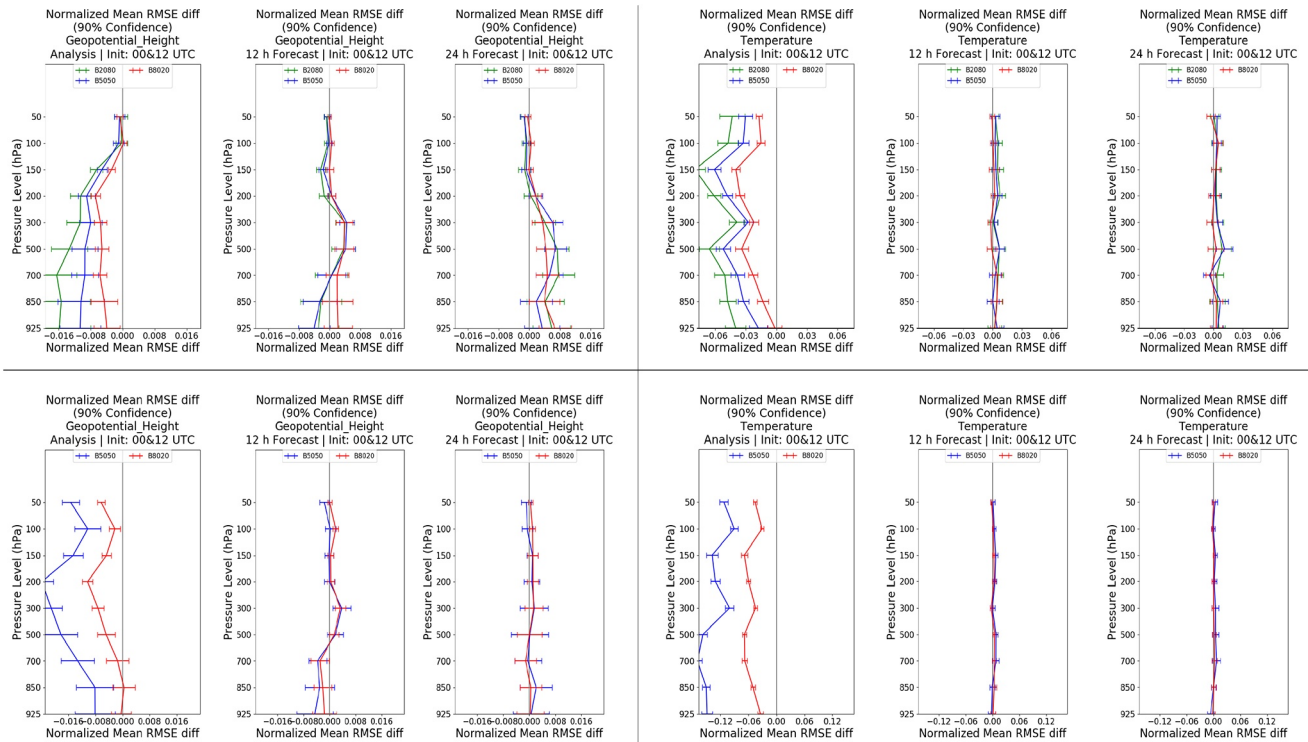


Figure 17. Difference in the root mean square error (RMSE) normalized by the mean forecast scores of: geopotential height (left six plots) and temperature (right six plots) fields against radiosonde observations, for the analysis (left-most in each block), 12-hr (middle in each block) and 24-hr (right-most in each block) forecasts starting from 00 to 12 UTC. The forecast differences are compared with and normalized by experiments run with **BS** against: **B8020** (red line), **B5050** (blue line), and **B2080** (green line). The plots are split into periods: March 2018 (top six plots) and March 2003 (bottom six plots). Each block of three plots, left to right, shows analysis, 12-hr and 24-hr forecasts. Positive values, to the right side of the vertical line at 0, represent an improvement over **BS**. There was an unresolvable issue in retrieving **B2080** March-2003 data.

Our line of scientific enquiry began with investigating if it was possible to capture weather regime change with our method of B-estimation, and if so, what caveats does it entail. We also wanted to know what impact our suggested B-estimation method would have on B-matrix statistics, DA system and forecast quality overall. In conclusion, it is possible to sufficiently estimate weather regime change given our setup, with clear improvements over **BS**, from the perspective of the DA system, the instantaneous increment and B-statistics. The HSS precipitation skill scores showed statistically significant improvements, however, the analysis and forecast skill scores show no marked improvement.

The case study showed that the statistics of the B-matrix: the time evolution of σ_b , and horizontal and vertical σ_b and σ_b^2 profiles, do indeed capture the changes instigated by weather regime changes from NAO— during March 2018. It is clear that simulating the March 2003 observation network in the March 2018 period, shows that the difference in observation network plays a significant role. To further support our hypothesis, we illustrated the potential spatial coverage differences, by taking a single assimilation-time snapshot between Aircraft observations in the middle of March 2003 and March 2018, Figure 8. March 2018 showed optimal positioning of spatial observations over the area of the pressure centers characterizing the advent of any weather regime. While this is important, the temporal continuity of these observations remains a vital point of consideration.

We also discussed the impact of varying α . It sufficiently increases the range of potential values that σ_b can take. This does not necessarily translate to better forecast skill scores, as can be seen for example, in Section 3.2.4, Figure 17. However, the range of σ_b values, while having some form of governance attributed to α , also depends on observation coverage as shown in Figures 11 and 10. It is shown that **B2080** and **B5050** allow for quicker and more severe drops in σ_b values at the cost of compromising the overall performance of the DA system and occasionally performing worse than **BS** (Table 2), whereas **B8020** exhibits a more restrained σ_b adjustment at times of weather regime change. **B8020** seemed to offer the right balance between DA system stability and performance

overall and allowed us to take the precaution of avoiding potentially superfluous 11-km-scale information from the daily component of the EDA to pollute the B-matrix statistics.

The method proposed here shows that there is clear improvement over the static B-matrix alternative, in terms of DA system (Table 2) and B-matrix statistics mirroring reality more closely. This is not reflected in the forecast skill quality however. This is not just a question of just the observations, since both the dynamic matrices and the static one had the same quality of observation networks.

The scope of our findings are illustrative at best, since we have only carried out a case study between two months over a ~40 year period. Another limitation was that in order to allow the observation network of March 2018 to mimic March 2003, we had to remove the aircraft observations for our experiments. Aircraft observations were shown to provide significant coverage over the European flow corridor and weather regime pressure centers. In light of our findings, the positive findings on the B-matrix statistics, and DA system diagnostics with the mild improvement in precipitation skill scores, there is enough promise to attempt to further the work here. This can be done by introducing wavelets for example, which would allow far better weather regime structure capture, and could perhaps lead to more decisive improvements in forecast skill.

Among potential further improvements, increasing the number of EDA members would reduce sampling error. Additionally, partitioning the length-scales where the EDAs can influence the B-matrix, for example, not allowing the daily 11 km EDA to have any input on the 5.5 km scales. Techniques avoiding the adjoint incumbency of 4DVAR are indeed seductive, and there is still plenty of room for pushing techniques such as 3DVAR, En3DVAR, and 4DVar further. In a reanalysis context however, the research is still in its infancy, and extensive testing of EnVar techniques would be required to ensure that improvements over non-EnVar techniques are indeed on offer.

At the date of writing this paper, CERRA production has been completed using the settings recommended by our research, an 80%–20% seasonal-daily split.

Conflict of Interest

The authors declare no conflicts of interest relevant to this study.

Data Availability Statement

The input and output data of the experiments described in the paper are freely available for research purposes from ECMWF's File Storage System (ECFS) by making a request via the ECMWF portal: <https://www.ecmwf.int/en/support>, and quoting the data set name: "CERRA B-matrix research data," and data set point of contact: martin.ridal@smhi.se.

Acknowledgments

The funding for the CERRA project comes from the Copernicus Climate Change Services (C3S_322 Lot 1) contract. The authors would like to thank members of the CERRA team for the fruitful discussions and experiences in producing CERRA: Semjon Schimanke, Eric Bazile, Patrick Le Moigne, Per Unden, Esbjörn Olsson, Per Dahlgren, and Lars Berggren. The author would also like to express extended gratitude to Loik Berre for the useful discussions, and to the two anonymous reviewers for their contributions towards greatly improving the paper.

References

- Bannister, R. N. (2008). A review of forecast error covariance statistics in atmospheric variational data assimilation. *Quarterly Journal of the Royal Meteorological Society*, 134(637), 1951–1970. <https://doi.org/10.1002/qj.339>
- Bartello, P., & Mitchell, H. L. (1992). A continuous three-dimensional model of short-range forecast error covariances. *Tellus A: Dynamic Meteorology and Oceanography*, 44(3), 217–235. <https://doi.org/10.3402/tellusa.v44i3.14955>
- Bengtsson, L., Kanamitsu, M., Kållberg, P., & Uppala, S. (1982). FGGE research activities at ECMWF. *Bulletin of the American Meteorological Society*, 63(3), 277–303. <https://doi.org/10.1175/1520-0477-63.3.277>
- Berre, L. (2000). Estimation of synoptic and mesoscale forecast error covariances in a limited-area model. *Monthly Weather Review*, 128(3), 644–667. [https://doi.org/10.1175/1520-0493\(2000\)128<0644:eosamf>2.0.co;2](https://doi.org/10.1175/1520-0493(2000)128<0644:eosamf>2.0.co;2)
- Bonavita, M., Isaksen, L., & Hólm, E. (2012). On the use of EDA background error variances in the ECMWF 4D-Var. *The Quarterly Journal of the Royal Meteorological Society*, 138(667), 1540–1559. <https://doi.org/10.1002/qj.1899>
- Bromwich, D. H., & Wang, S.-H. (2005). Evaluation of the NCEP–NCAR and ECMWF 15- and 40-yr reanalyses using rawinsonde data from two independent Arctic field experiments. *Monthly Weather Review*, 133(12), 3562–3578. <https://doi.org/10.1175/mwr3043.1>
- Brousseau, P., Berre, L., Bouttier, F., & Desroziers, G. (2011). Background-error covariances for a convective-scale data-assimilation system: AROME-France 3d-Var. *Quarterly Journal of the Royal Meteorological Society*, 137(655), 409–422. <https://doi.org/10.1002/qj.750>
- Brousseau, P., Berre, L., Bouttier, F., & Desroziers, G. (2012). Flow-dependent background-error covariances for a convective-scale data assimilation system. *Quarterly Journal of the Royal Meteorological Society*, 138(663), 310–322. <https://doi.org/10.1002/qj.920>
- Bruyninx, C., Legrand, J., Fabian, A., & Pottiaux, E. (2019). GNSS metadata and data validation in the EUREF permanent network. *GPS Solutions*, 23(4). <https://doi.org/10.1007/s10291-019-0880-9>
- Cardinali, C., Pezzulli, S., & Andersson, E. (2004). Influence-matrix diagnostic of a data assimilation system. *Quarterly Journal of the Royal Meteorological Society*, 130(603), 2767–2786. <https://doi.org/10.1256/qj.03.205>

- Dee, D. P., Uppala, S. M., Simmons, A. J., Berrisford, P., Poli, P., Kobayashi, S., et al. (2011). The era-interim reanalysis: Configuration and performance of the data assimilation system. *Quarterly Journal of the Royal Meteorological Society*, 137(656), 553–597. <https://doi.org/10.1002/qj.828>
- Derber, J., & Bouttier, F. (1999). A reformulation of the background error covariance in the ECMWF global data assimilation system. *Tellus A: Dynamic Meteorology and Oceanography*, 51(2), 195–221. <https://doi.org/10.3402/tellusa.v51i2.12316>
- El-Said, A. (2015). *Conditioning of the weak-constraint variational assimilation problem for numerical weather prediction (PhD Thesis)*. University of Reading, Whiteknights.
- Fisher, M. <https://www.ecmwf.net/sites/default/files/elibrary/2003/9404-background-error-covariance-modelling.pdf>
- Hägmark, L., Ivarsson, K.-L., Gollvik, S., & Olofsson, P.-O. (2000). Mesan, an operational mesoscale analysis system. *Tellus A: Dynamic Meteorology and Oceanography*, 52(1), 2–20. <https://doi.org/10.3402/tellusa.v52i1.12250>
- Hersbach, H., Bell, B., Berrisford, P., Hirahara, S., Horányi, A., Muñoz-Sabater, J., et al. (2020). The ERA5 global reanalysis. *Quarterly Journal of the Royal Meteorological Society*, 146(730), 1999–2049. <https://doi.org/10.1002/qj.3803>
- Hollingsworth, A., & Lönnberg, P. (1986). The statistical structure of short-range forecast errors as determined from radiosonde data. Part I: The wind field. *Tellus A*, 38A(2), 111–136. <https://doi.org/10.1111/j.1600-0870.1986.tb00460.x>
- Isaksen, L., Fisher, M., & Berner, J. (2007). Use of analysis ensembles in estimating flow-dependent background error variance. In *Proc. ECMWF workshop on flow-dependent aspects of data assimilation* (pp. 65–86). <https://www.ecmwf.int/sites/default/files/elibrary/2007/10127-use-analysis-ensembles-estimating-flow-dependent-background-error-variance.pdf>
- Masson, V., Le Moigne, P., Martin, E., Faroux, S., Alias, A., Alkama, R., et al. (2013). The SURFEXv7. 2 land and ocean surface platform for coupled or offline simulation of earth surface variables and fluxes. *Geoscientific Model Development Discussions*, 5. <https://doi.org/10.5194/gmdd-5-3771-2012>
- Palmer, T. N. (2001). A nonlinear dynamical perspective on model error: A proposal for non-local stochastic-dynamic parametrization in weather and climate prediction models. *Quarterly Journal of the Royal Meteorological Society*, 127(572), 279–304. <https://doi.org/10.1002/qj.49712757202>
- Parrish, D. F., & Derber, J. C. (1992). The national meteorological center's spectral statistical-interpolation analysis system. *Monthly Weather Review*, 120(8), 1747–1763. [https://doi.org/10.1175/1520-0493\(1992\)120<1747:tnmcss>2.0.co;2](https://doi.org/10.1175/1520-0493(1992)120<1747:tnmcss>2.0.co;2)
- Parrish, D. F., Derber, J. C., Purser, R. J., Wu, W.-S., & Pu, Z.-X. (1997). The NCEP global analysis system: Recent improvements and future plans (Special issue: Data assimilation in meteorology and oceanography: Theory and practice). *Journal of the Meteorological Society of Japan. Ser. II*, 75(1B), 359–365. https://doi.org/10.2151/jmsj1965.75.1b_359
- Phillips, N. A. (1986). The spatial statistics of random geostrophic modes and first-guess errors. *Tellus A: Dynamic Meteorology and Oceanography*, 38(4), 314–332. <https://doi.org/10.3402/tellusa.v38i4.11721>
- Poli, P., Hersbach, H., Dee, D. P., Berrisford, P., Simmons, A. J., Vitart, F., et al. (2016). ERA-20c: An atmospheric reanalysis of the twentieth century. *Journal of Climate*, 29(11), 4083–4097. <https://doi.org/10.1175/jcli-d-15-0556.1>
- Vautard, R. (1990). Multiple weather regimes over the North Atlantic: Analysis of precursors and successors. *Monthly Weather Review*, 118(10), 2056–2081. [https://doi.org/10.1175/1520-0493\(1990\)118<2056:mwrotn>2.0.co;2](https://doi.org/10.1175/1520-0493(1990)118<2056:mwrotn>2.0.co;2)
- Wang, Z. Q., & Randriamampianina, R. (2021). The impact of assimilating satellite radiance observations in the Copernicus European Regional Reanalysis (CERRA). *Remote Sensing*, 13(3), 426. <https://doi.org/10.3390/rs13030426>